Investigating dynamical effect of an $m = 1$ lopsidedness on measuring bar pattern speed

M.Sc. Thesis

by

KANISHKA GAUTAM



DEPARTMENT OF ASTRONOMY, ASTROPHYSICS & SPACE ENGINEERING

INDIAN INSTITUTE OF TECHNOLOGY INDORE

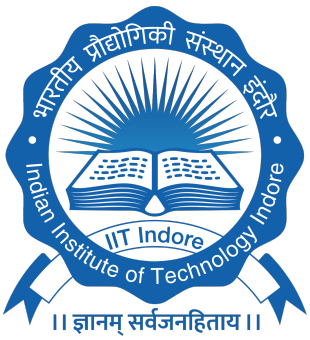
May 17, 2026

Investigating dynamical effect of an $m = 1$ lopsidedness on measuring bar pattern speed

A THESIS

Submitted in partial fulfillment of the requirements for the award of the degree
of
Master of Science

by
KANISHKA GAUTAM



DEPARTMENT OF ASTRONOMY, ASTROPHYSICS & SPACE ENGINEERING

INDIAN INSTITUTE OF TECHNOLOGY INDORE

MAy 17, 2026

INDIAN INSTITUTE OF TECHNOLOGY INDORE

CANDIDATE'S DECLARATION

I hereby certify that the work which is being presented in the thesis entitled **INVESTIGATING DYNAMICAL EFFECT OF AN *m=1* LOPSIDEDNESS ON MEASURING BAR PATTERN SPEED** in the partial fulfillment of the requirements for the award of the degree of **MASTER OF SCIENCE** and submitted in the **DEPARTMENT OF ASTRONOMY, ATROPHYSICS & SPACE ENGINEERING, Indian Institute of Technology Indore**, is an authentic record of my own work carried out during the time period from June 2025 to May 2026 under the supervision of Dr. Soumavo Ghosh, Assistant Professor, Department of Astronomy, Astrophysics and Space Engineering

The matter presented in this thesis has not been submitted by me for the award of any other degree of this or any other institute.

Kanishka.

07-05-2026

Signature of the student with date
(KANISHKA GAUTAM)

This is to certify that the above statement made by the candidate is correct to the best of my knowledge.

Soumavo Ghosh.

07.05.2026

Signature of the Supervisor of

M.Sc. thesis (with date)

(Dr. SOUMAVO GHOSH)

KANISHKA GAUTAM has successfully given her M.Sc. Oral Examination held on **05-05-2026**.

Soumavo Ghosh.

Signature(s) of Supervisor(s) of MSc thesis
Date: 07.05.2026

Manoneeta Chakraborty

Programme Coordinator, M.Sc.
Date: 08/05/2026

Manoneeta Chakraborty

Convenor, DPGC
Date: 08/05/2026

HoD, DAASE
Date: 08/05/2026

ACKNOWLEDGEMENTS

I sincerely thank Dr. Soumavo Ghosh for his continuous guidance, motivation, and valuable feedback throughout this project. His insights and encouragement helped me at every stage of my work. The weekly lab discussions created a wonderful learning atmosphere. These sessions allowed me to learn many things and improve my understanding during my M.Sc. project. I also thank my lab mates and friends for their support and encouragement, which kept me motivated throughout this journey.

I acknowledge generous support from IIT-Indore through Dr. Soumavo Ghosh's YFRSG-Dream-PRIUS funding (IITI/YFRSG-Dream-PRIUS/Phase-I/2025-26/06). I am grateful for providing the necessary resources to complete this work. I would like to extend my sincere thanks to the faculty members and staff of IIT Indore for providing a supportive academic environment and necessary facilities.

My heartfelt thanks to my parents for their love, sacrifices, and belief in me, and to my siblings for their understanding and support. I also acknowledge everyone who directly or indirectly contributed to this work. Any omission is unintentional and does not diminish my appreciation.

Kanishka Gautam
2403121005
IIT Indore

In memory of my beloved dog, Rocky...

ABSTRACT

Bars are among the most prominent structures in disc galaxies, including our own Milky Way, which rotates with a well-defined pattern speed. This pattern speed is a key dynamical parameter, as it governs how the bar exchanges angular momentum with the surrounding disc and halo, thereby influencing the long-term evolution of the galaxy. Measuring this quantity accurately is therefore essential for understanding galactic dynamics.

The Tremaine-Weinberg (TW) method is widely used to estimate the bar pattern speed from observational data. It is quite a straightforward model-independent method; however, it relies on an important assumption that the disc is axisymmetric outside the bar region. In reality, many galaxies show clear departures from axisymmetry, particularly in the form of an $m = 1$ lopsidedness in the outer disc, often accompanied by spiral features. This raises an important question regarding the reliability of TW-based measurements in such systems.

The aim of this work is to investigate how the presence of an $m = 1$ lopsidedness affects the measurement of the bar pattern speed using the TW method. To address this, we analyse N-body simulations of minor merger systems from the GalMer database, where such asymmetries naturally develop in the outer regions of the disc. The true bar pattern speed is determined using the DSS method, based on the temporal evolution of an $m = 2$ Fourier phase, providing a robust reference against which the TW measurements can be compared.

We first validate the TW method for an axisymmetric case, where it successfully recovers the true pattern speed. We then progressively examine systems with increasing strength of lopsidedness, ranging from weak to intermediate and strong asymmetry. In the weak regime, the TW method continues to provide values close to the true pattern speed, with only small deviations. However, as the strength of lopsidedness increases, the behaviour changes noticeably. The TW relation shows increasing scatter, and the derived pattern speeds begin to deviate from the true values. In cases with intermediate and strong lopsidedness, these deviations become significant, and the results can vary widely, indicating a loss of reliability.

Overall, this study demonstrates that an $m = 1$ lopsidedness introduces a systematic bias in TW-based measurements of the bar pattern speed. While the method performs well in symmetric or weakly asymmetric discs, its accuracy decreases as the level of asymmetry increases, leading to large scatter and inconsistent values. Since lopsidedness is common in real galaxies, these results highlight an important limitation of the TW method in idealised conditions and provide a clearer understanding of how such measurements should be interpreted.

TABLE OF CONTENTS

LIST OF FIGURES iii

LIST OF TABLES vii

1 Introduction 1
- 1.1 Occurrence of bars in real galaxies . . . 1
- 1.2 Bar formation in simulated galaxies & their dynamical effect . . 3
- 1.3 Observable properties of bars . . . 4
  - 1.3.1 Strength of the bar . . . 5
  - 1.3.2 Bar Length . . . 6
  - 1.3.3 Bar pattern speed . . . 7
- 1.4 Pattern speed measurement of bars & the associated challenges . 8
- 1.5 Formation of lopsidedness and co-existence with bars . . . 9
- 1.6 Scientific goal of the thesis . . . 11

2 The Tremaine-Weinberg Method 13
- 2.1 Formulation of the TW method . . . 14
- 2.2 Assumptions of the TW method . . . 15
- 2.3 Sources of Error and Uncertainties . . . 16
  - 2.3.1 Galaxy Inclination Effects . . . 16
  - 2.3.2 Bar Orientation Relative to the Disc . . . 16
  - 2.3.3 Slit Placement . . . 16
  - 2.3.4 Disc Position Angle . . . 17
  - 2.3.5 Galaxy Centre Determination . . . 17
  - 2.3.6 Instrumental and Observational Limitations . . . 17
  - 2.3.7 Effects of Noise and Non-Axisymmetric Structures . . . 17

3 The GaLMer database 19
- 3.1 Equilibrium Galaxy Model . . . 19
- 3.2 Orbital Parameters . . . 20
- 3.3 Temporal Evolution . . . 21

4 Results 23
- 4.1 Characterisation of selected minor merger models . . . 23
  - 4.1.1 Orbital separation over time . . . 23
- 4.2 Quantification of m=2 bar and m=1 lopsidedness . . . 25
- 4.3 True bar pattern speed measurement - DSS method . . . 27
- 4.4 Bar pattern speed via TW Method . . . 29
  - 4.4.1 Creating the LOS maps from intrinsic particle distribution 30
  - 4.4.2 The case with no lopsidedness – sanity check . . . 31
  - 4.4.3 The Case with Weak lopsidedness . . . 32
  - 4.4.4 The Case with Intermediate lopsidedness . . . 33

4.4.5 The case with Strong lopsidedness 35

5 Summary and Future scope **39**

REFERENCES **41**

LIST OF FIGURES

1.1 Prominent examples of $m = 2$ barred galaxies in the local Universe. *Left to right*: NGC 1300, M 109 (*top panel*), and NGC 1365, NGC 1097 (*bottom panel*). *Image credit*: ESO-VLT, NASA/ESA-HST, STScI, Cerro Tololo Inter-American Observatory. 1

1.2 An artist's impression of our Milky Way: a central stellar bar and spiral features in the outer stellar disc. *Image Credit*: NASA/JPL-Caltech. 2

1.3 *Presence of an $m = 1$ lopsidedness in observed galaxies. Top left panel:* M101 showing a grey-scale map of its lopsided H I intensity (Braun, 1995). *Top right panel:* H I intensity contours overlaid on an optical image of NGC 2841, revealing its lopsided gas disc (Bosma, 1981). *Bottom left panel:* H I contours superimposed on an optical image of NGC 4654, another example of a lopsided disc (Phookun and Mundy, 1995). *Bottom right panel:* Combined contour and grey-scale map of the H I intensity in UGC 7989 (E. Noordermeer et al., 2005). 9

3.1 Orbital configuration implemented in the GalMer simulations, taken from Chilingarian et al. (2010). The collision is initialised with the total orbital angular momentum aligned along the z-axis, and the galactic centres positioned on the x-axis at the start. The intrinsic angular momenta (spins) of the two galaxies are indicated by the blue and red arrows, parameterised by the spherical angles (i_1, Φ_1) and (i_2, Φ_2), respectively. 21

4.1 Face-on stellar surface-density maps of the combined host (gSa) and satellite (dE0) system are shown at various evolutionary stages for the two minor-merger models, 'gSadE001dir33' (*top panels*) and 'gSadE006ret33' (*bottom panels*). Black lines mark contours of equal surface density, while the colour bar represents the stellar surface density (arbitrary units) for each of the two models. 23

4.2 *Time evolution of orbital separation between the host and satellite:* The separation (in kpc) between the centres of the satellite (*dE0*) and the host galaxy (*gSa*) is shown as a function of time for the two minor merger models *gSadE001dir33* (in red) and *gSadE006ret33* (in blue). The curves trace the orbital decay, with successive dips indicating pericentric passages and the gradual decrease in separation as the merger progresses. 25

4.3 Radial profiles of the $m = 2$ and $m = 1$ Fourier coefficients (each normalised by the $m = 0$ component), calculated using Eq. 1.3, are shown as a function of time in Gyr (indicated by the colour bar) for the two minor-merger models 'gSadE001dir33' and 'gSadE006ret33', respectively, where $R_{\rm d}$ is the disc scale length, taken to be 3 kpc. 26

4.4 *Correlation between median and integrated an $m = 1$ amplitudes in inner and outer disc regions:* The top panels show the outer disc ($5 \leq R/R_d \leq 7$), while the bottom panels correspond to the inner disc ($0 \leq R/R_d \leq 5$), for the two models 'gSadE001dir33' (left) and 'gSadE006ret33' (right). Each point represents a different snapshot, with colour indicating the time evolution. The region shows a tighter correlation, while the inner region displays increased scatter due to the presence of a spiral arm. The Pearson correlation coefficient, ρ, is shown in each panel. 27

4.5 Temporal evolution of the pattern speed $\Omega_{\rm bar}$ (in km s^{-1} kpc^{-1}) over time (in Gyr) for two distinct minor merger models, 'gSadE001dir33' and 'gSadE006ret33'. Magenta arrows show the epochs of pericentre passage for both models. 29

4.6 Line-of-sight (LOS) maps constructed from the intrinsic particle distribution. The top panels show the projected surface density maps, while the bottom panels show the corresponding LOS velocity maps. The columns represent inclination angles of 15°, 30°, 45°, and 60° respectively. The cross symbol '×'(in blue) marks the photometric centre of the galaxy. Black contours denote constant levels, and the colour bars indicate the plotted quantity. Shown for the model 'gSaadE001dir33' 31

4.7 *Left panel* shows $\Omega_{\rm bar,TW}$ as a function of slit half-length ($L_{\rm half}$, stabilising beyond $\sim$ 14 pixels, taken as the optimal length. *Right panel* shows $\Omega_{\rm bar,TW}$ as a function of disc inclination, stabilising over a range around 15°. Shaded regions denote the stable ranges. 31

4.8 *Case with no lopsidedness: Left* and *middle* panels show the line-of-sight ($i = 15°$) density and velocity maps, respectively. Black solid lines denote the contours of constant density (*left panel*) and $V_{\rm LOS}$ (*middle panel*), respectively. Horizontal black lines denote the slit positions and '×' denotes the photometric centre. *Right panel:* luminosity-weighted position $\langle X \rangle$ and the y-axis represents the luminosity-weighted velocity $\langle V \rangle$ as well as the best-fit slope to derive the bar pattern speed ($\Omega_{\rm bar,TW}$) via the TW method. In the absence of lopsidedness, the TW method recovers the true bar pattern speed ($\Omega_{\rm bar,true}$) within 2 km s^{-1} kpc^{-1}. 32

4.9 *Case with weak lopsidedness: Left* and *middle* panels show the line-of-sight ($i = 15°$) density and velocity maps, respectively. Black solid lines denote the contours of constant density (*left panel*) and $V_{\rm LOS}$ (*middle panel*), respectively. Horizontal black lines denote the slit positions and '×' denotes the photometric centre. *Right panel:* luminosity-weighted position $\langle X \rangle$ and the y-axis represents the luminosity-weighted velocity $\langle V \rangle$ as well as the best-fit slope to derive the bar pattern speed ($\Omega_{\rm bar,TW}$) via the TW method. In weak lopsidedness, TW closely matches the true value with a small offset, a slight overestimation in 'gSadE006ret33' and underestimation in 'gSadE001dir33'. . . . 33

4.10 *Case with intermediate lopsidedness: Left* and *middle* panels show the line-of-sight ($i = 15°$) density and velocity maps, respectively. Black solid lines denote the contours of constant density (*left panel*) and $V_{\rm LOS}$ (*middle panel*). Horizontal black lines denote the slit positions and '×' denotes the photometric centre. *Right panel:* luminosity-weighted position $\langle X \rangle$ and luminosity-weighted velocity $\langle V \rangle$ with the best-fit slope giving $\Omega_{\rm bar,TW}$. In intermediate lopsidedness, where slit orientations are not directly aligned with the lopsided component, the TW method still shows noticeable deviation from the true value. . . 34

4.11 *Case with strong lopsidedness: Left* and *middle* panels show the line-of-sight ($i = 15°$) density and velocity maps, respectively. Black solid lines denote the contours of constant density (*left panel*) and $V_{\rm LOS}$ (*middle panel*). Horizontal black lines denote the slit positions and '×' denotes the photometric centre. *Right panel:* luminosity-weighted position $\langle X \rangle$ and luminosity-weighted velocity $\langle V \rangle$ with the best-fit slope giving $\Omega_{\rm bar,TW}$. In strong lopsidedness, TW deviates significantly from the true value, showing large overestimation in 'gSadE006ret33' and underestimation in 'gSadE001dir33'. 35

4.12 *Comparison of TW-derived and true bar pattern speeds:* Left and right panels show the relation between the TW-derived bar pattern speed, $\Omega_{\rm bar,TW}$, and the true value, $\Omega_{\rm bar,True}$, for the 'gSadE001dir33' and 'gSadE006ret33' models, respectively. Each point corresponds to a different snapshot, with colour indicating the time evolution of the system. The dashed line denotes the one-to-one relation, while the shaded region highlights the expected range of agreement. 37

LIST OF TABLES

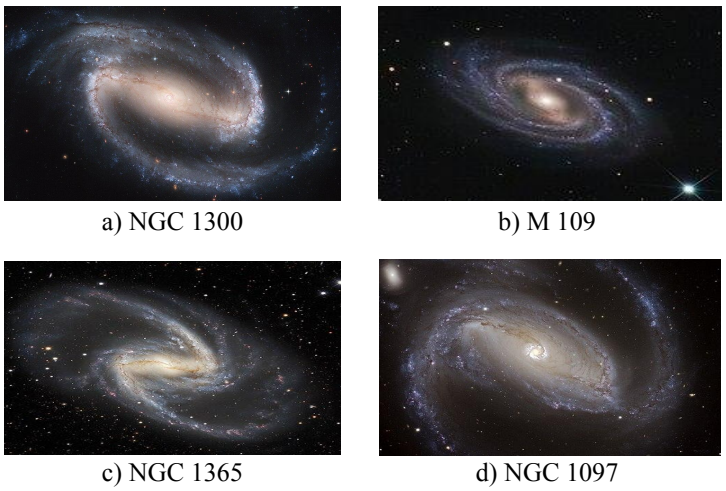
4.1 Key parameters of the selected GalMer minor-merger models (Chilingarian et al., 2010). 24

Chapter 1

Introduction

1.1 Occurrence of bars in real galaxies

Bars are one of the most frequent and dynamically prominent non-axisymmetric structures that we encounter in the central region of disc galaxies. They are very common and are characterised by their long extent, high brightness, and strong gravitational influence. As a result, they play a significant role in shaping up the galaxy's structure and influence the movement of stars and gas within it. Figure 1.1 shows a few prominent examples of barred galaxies from observations.



a) NGC 1300 b) M 109

c) NGC 1365 d) NGC 1097

Figure 1.1: Prominent examples of $m = 2$ barred galaxies in the local Universe. *Left to right*: NGC 1300, M 109 (*top panel*), and NGC 1365, NGC 1097 (*bottom panel*). *Image credit*: ESO-VLT, NASA/ESA-HST, STScI, Cerro Tololo Inter-American Observatory.

Observations from large optical and near-infrared surveys showed that the number of disc galaxies with bars depends on the wavelength we observe. In optical images, only about 50% of disc galaxies appear to have a bar, because dust and bright star-forming regions can obscure part of the bar structure. When these same galaxies are examined at near-infrared wavelengths, where the impact of interstellar dust is greatly reduced, and the emission from older stellar populations becomes far more prominent, a very different picture emerges. In this part of the electromagnetic spectrum, the proportion of disc galaxies hosting bars increases markedly, with studies consistently finding that nearly two-thirds of all disc galaxies in the nearby Universe exhibit bar structures (e.g., Aguerri, 1999a; Menendez-Delmestre et al., 2007; Barazza, Jogee, and Marinova, 2008; Aguerri, Méndez-Abreu, and E. M. Corsini, 2009; Nair and Abraham, 2010; Masters et al., 2011; Kruk et al., 2017). Studies of the early universe show that a significant number of disc galaxies at high redshift ($z \sim 1$) possess strong and noticeable bar structures. However, studies have uncovered a clear pattern that the percentage of galaxies that have a bar becomes lower as we look further back

in time to higher redshifts. Multiple studies have shown that the proportion of barred disc galaxies declines when moving to higher redshifts. This trend, first hinted by Jogee et al. (2004), has since been strongly reinforced by the results of Sheth et al. (2008) and Melvin et al. (2014). Remarkably, new data from the James Webb Space Telescope (JWST) have pushed this picture even further, showing that well-defined bars were already present in some galaxies as early as $z \sim 3$ (e.g., Costantin et al., 2023; Guo, Jogee, Finkelstein, et al., 2023; Le Conte et al., 2024). In addition to the JWST, the *Euclid* mission, launched in 2023, is now providing early data releases that enable large-scale statistical studies of galaxy populations and evolution (Collaboration et al., 2026). More recently, the JWST analyses extend this redshift range, with Guo, Jogee, Wise, et al. (2025) showed clear bar structures up to $z \sim 4$, although the observed bar fraction at these early epochs is still low (around 10% or less). Moreover, according to Géron et al. (2025), the proportion of barred galaxies falls to nearly 3% within the redshift interval $3 < z < 4$. Together, these studies indicate that bar formation had already begun in the early Universe, suggesting that bar-driven evolution may start much earlier than previously expected. Numerous N-body experiments have shown that disc galaxies are capable of generating bars through their own internal dynamical processes (e.g., F. Combes and Sanders, 1981; J A Sellwood and Wilkinson, 1993; Victor P. Debattista and J. A. Sellwood, 2000; Athanassoula, 2003). Furthermore, cosmological simulations indicate that the onset of bar formation generally occurs near $z \sim 1$, with some simulations predicting bar development even earlier (e.g., Kraljic, Frédéric Bournaud, and Martig, 2012; Rosas-Guevara et al., 2022). At these early stages in the universe, galaxy discs are believed to be very clumpy and unstable. They are expected to contain a lot of gas, have highly turbulent or 'hot' motions, and are supported by a thick and massive disc component. Despite these challenging conditions, recent N-body simulations that include both a thin disc and a thick disc show that bars and box-shaped bulges can still form, these structures do not require external triggers; instead, they arise naturally from the disc's own internal gravitational forces (Ghosh, Soumavo et al., 2023). Building on this, Ghosh, Fragkoudi, et al. (2024) demonstrated that the formation of boxy/peanut bulges remains robust even in the presence of a massive thick disc, although the growth rate and vertical structure of the boxy bulge can be significantly influenced by the thickness and kinematics of the disc. Their results highlight that thick discs do not suppress bar-driven vertical instabilities but instead modulate the subsequent evolution of boxy/peanut bulges.

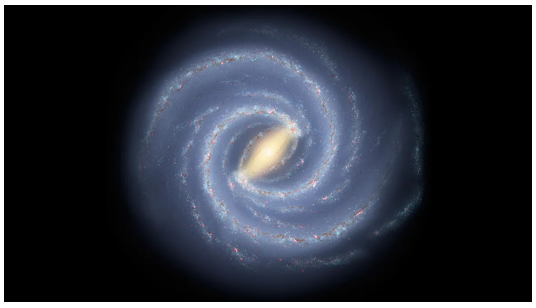


Figure 1.2: An artist's impression of our Milky Way: a central stellar bar and spiral features in the outer stellar disc. *Image Credit*: NASA/JPL-Caltech.

Observations have shown that our own galaxy, the Milky Way, hosts a prominent stellar bar in its central region. This result has been supported by numerous investigations and studies over the years (e.g. Liszt and Burton, 1980; James Binney et al., 1991; Hammersley et al., 2000; Wegg and Gerhard, 2013). As shown in Figure 1.2, the Milky Way has a bar at the centre with its prominent spiral arms extending from either end.

1.2 Bar formation in simulated galaxies & their dynamical effect

A stellar bar forms when the disc of a galaxy becomes unstable to small, non-axisymmetric disturbances in its own gravity. In this situation, the disc is not breaking down; instead, the bar grows naturally as one type of gravitational instability that can develop in a cold, rotating disc (e.g., A. Toomre, 1981; Athanassoula, 2002; J. A. Sellwood, 2014). This happens when two main conditions are met. First, the disc must have enough mass; if the disc is too light, it cannot form a bar (Efstathiou, Lake, and Negroponte, 1982; J. A. Sellwood, 1989). Secondly, the stars in the disc must move in an ordered manner. When stars follow nearly circular paths with little random motion, the disc is said to be dynamically cold, which strongly favours bar formation (A. Toomre, 1964; Athanassoula, 2003). When both conditions are present, even a tiny clump of stars can trigger the process. If a few stars happen to be closer together than average, their local gravitational pull becomes slightly stronger, creating a small over-density (Julian and Alar Toomre, 1966). This marginal enhancement in gravity is sufficient to perturb nearby stellar orbits, causing stars to deviate from circular motion and adopt more elongated, oval-shaped trajectories. As the galaxy rotates, these perturbations grow coherently, and an increasing number of stars become trapped in aligned elongated orbits (Contopoulos, 1980; J A Sellwood and Wilkinson, 1993). This alignment leads to a self-reinforcing feedback loop, the elongated stellar orbits enhance the non-axisymmetric gravitational potential, which in turn captures additional stars into the bar structure. This runaway instability was first robustly demonstrated in numerical simulations by Ostriker and Peebles (1973) and has since been confirmed by numerous high-resolution simulations (Athanassoula, 2002; J. A. Sellwood, 2012). The process continues until the inner disc undergoes substantial rearrangement, resulting in the emergence of a strong, coherent bar that rotates as a single, long-lived pattern within the galaxy (Athanassoula, 2003; J. A. Sellwood, 2014).

The growth and stability of a stellar bar are governed by a fundamental physical process: the large-scale redistribution of angular momentum (e.g., Athanassoula, 2003; Victor P. Debattista, Mayer, et al., 2006; J. A. Sellwood, 2012). When a bar starts to develop, it behaves like a large-scale conveyor system within the galaxy. It gradually moves angular momentum away from the inner parts of the disc and delivers it to the outer disc and even to the dark matter halo that surrounds the galaxy (Victor P. Debattista, Mayer, et al., 2006). This transfer occurs through gravitational torques exerted at orbital resonances, particularly at corotation, where the stars co-rotate with the bar, having the same angular frequency as the bar pattern (for more details, read section 1.4), and at the Lindblad resonances, where orbital frequencies match the bar's perturbation frequency. The effectiveness of this angular-momentum

transfer strongly depends on the nature of the dark matter halo. Halos that rotate slowly and have a moderate level of concentration are the most capable of absorbing angular momentum. This process not only enables the bar to strengthen and maintain its structure but also fundamentally alters the global dynamics of the host galaxy (Athanassoula, 2003; J. A. Sellwood, 2012). This inward movement of gas frequently triggers strong episodes of star formation in the galaxy's central region and plays a major role in building up the central bulge (e.g., Spinoso et al., 2016; Donohoe-Keyes et al., 2019; George, Subramanian, and Paul, 2019). In this way, stellar bars are primary drivers of the slow, internal transformation known as secular evolution, playing a dynamic role in reshaping their galaxies by channelling mass and angular momentum to different regions.

Once a stable bar is established, its non-axisymmetric gravitational potential drives the secular evolution of the host galaxy by exerting gravitational torques that remove angular momentum from the interstellar gas. As a result, gas deviates from circular orbits and streams inward along the bar, typically offset toward its leading edges (e.g., Athanassoula, 1992; Spinoso et al., 2016; George, Subramanian, and Paul, 2019). Shock-induced dissipation along these paths further enhances angular momentum loss, allowing gas to flow efficiently from the outer disc into the central regions, increasing central gas densities and fuelling star formation and the buildup of central mass concentrations (Dimitri A. Gadotti, 2011; Sormani, James Binney, and Magorrian, 2015). At the same time, the bar redistributes angular momentum across the galaxy, transferring it outward to the outer disc and dark matter halo while also sustaining spiral structure through coupling with disc resonances (Athanassoula, 1992; J. Binney and Tremaine, 2008; J A Sellwood and Wilkinson, 1993; Athanassoula, 2003). This process also heats the stellar disc, increasing random motions and leading to gradual vertical thickening (Kormendy and Robert C. Kennicutt, 2004; Kanak Saha, Tseng, and Taam, 2010). The accumulated central gas can support star formation, contribute to pseudobulge growth, and potentially trigger nuclear or AGN activity (e.g., Kormendy and Robert C. Kennicutt, 2004; Dimitri Alexei Gadotti, 2004; Donohoe-Keyes et al., 2019). In addition, bars may undergo vertical buckling instabilities that form boxy/peanut-shaped bulges and reshape the inner structure (F. Combes, Dupraz, and Gerin, 1990; Raha et al., 1991; Ghosh and Paola Di Matteo, 2024). Over longer timescales, continued angular momentum exchange leads to a gradual slowdown and strengthening of the bar, further modifying the galaxy's orbital structure and kinematics (Victor P. Debattista and J. A. Sellwood, 2000; Athanassoula, 2003). Taken together, bar-driven gas inflow, spiral structure formation, disc heating and thickening, buckling-driven bulge formation, and continual angular momentum redistribution establish bars as one of the primary engines of secular evolution, capable of transforming galaxies from their central regions to their outer discs over billions of years.

1.3 Observable properties of bars

Stellar bars have several key properties that we can observe and measure to understand their structure and how they affect galaxies. The three most fundamental of these are the *bar strength*, the *bar length*, and the *bar pattern speed*. Each parameter reveals different aspects of bar formation, evolution, and interaction

with the surrounding galactic components.

Past observational studies have shown that the properties of stellar bars, as well as the overall fraction of galaxies that host them, vary across different types of galaxies. These characteristics have been found to systematically change with two key galactic properties: the total stellar mass of the galaxy and its Hubble type classification. In other words, the prevalence of bars and their specific features depends on whether a galaxy is a massive spiral or a smaller dwarf and whether it is classified as, for example, an Sa or an Sd type. This observed variation has been reported in a number of key studies, such as those by Aguerri, Méndez-Abreu, and E. M. Corsini (2009), Nair and Abraham (2010), Barway, Wadadekar, and Kembhavi (2011), Dimitri A. Gadotti (2011), and Peter Erwin (2018).

1.3.1 Strength of the bar

Bar strength quantifies how strongly the bar deviates from the axial symmetry and is measured using several observational and simulation-based techniques. Among observational methods, one of the most widely used is the *ellipticity measurement* method, which estimates bar strength from the flattening of fitted elliptical isophotes on galaxy images. In this approach, a higher ellipticity value corresponds to a more elongated and therefore, a stronger bar (Aguerri, 1999b; Marinova and Jogee, 2007). Another commonly used observational indicator is the *Surface Brightness Ratio* technique, which measures the strength of a bar by comparing the peak surface brightness within the bar to the lowest surface brightness found in the inter-bar region. A larger ratio corresponds to a stronger and more visually dominant bar (B. G. Elmegreen and D. M. Elmegreen, 1985). A more physically motivated approach is the *bar torque* method, in which the bar strength is quantified using the maximum ratio of the tangential force to the mean axisymmetric radial force in the disc, commonly denoted as Q_b. This method provides a direct estimate of the non-axisymmetric gravitational forcing induced by the bar and has been widely applied in both observational and theoretical studies (F. Combes and Sanders, 1981; E. Laurikainen, H. Salo, and Rautiainen, 2002).

A more detailed and physically motivated implementation of this approach is based on Fourier analysis of the surface brightness distribution. The *Fast Fourier Transform (FFT)* technique decomposes the two-dimensional light distribution into its Fourier modes, where the amplitude of the $m = 2$ component measures the bar's characteristic bi-symmetric structure (Garcia-Gómez et al., 2017). This Fourier decomposition approach is especially widely used in numerical simulations and has been applied in many previous works (e.g., Eija Laurikainen, Heikki Salo, and Ronald Buta, 2004; Eija Laurikainen, Heikki Salo, and Ronald Buta, 2005; H. Salo et al., 2010).

In the Fourier decomposition method, the projected surface density distribution of a galaxy is expressed as a Fourier series. This technique is used to calculate the bar strength from the amplitude of the $m = 2$ Fourier moment (e.g., Aguerri, 1999b; Victor P. Debattista and J. A. Sellwood, 2000; Athanassoula, 2003; Ghosh, Kanak Saha, Di Matteo, et al., 2021; Ghosh, Kanak Saha, Jog, et al., 2022). Here, m represents the Fourier moment, where the $m = 2$ com-

ponent specifically corresponds to the bar's two-armed symmetry as shown in Figure 1.1. The strength of the bar is quantified by the ratio A_2/A_0, where A_2 is the amplitude of this $m = 2$ component and A_0 is the axisymmetric component of the disc light distribution (e.g., H. Salo et al., 2010; Ghosh, Kanak Saha, Di Matteo, et al., 2021; Ghosh, Soumavo et al., 2023) given as below,
In this method, the projected surface density $\Sigma(r, \theta)$ is decomposed as:

$$a_m(r) = \frac{1}{\pi} \int_0^{2\pi} \Sigma(r, \theta) \cos(m\theta)\, d\theta, \tag{1.1}$$

$$b_m(r) = \frac{1}{\pi} \int_0^{2\pi} \Sigma(r, \theta) \sin(m\theta)\, d\theta. \tag{1.2}$$

The amplitude of the $m = 2$ mode is then

$$A_2(r) = \sqrt{a_2^2(r) + b_2^2(r)}, \tag{1.3}$$

and the corresponding phase angle is

$$\Phi_2(r) = \arctan\left(\frac{b_2(r)}{a_2(r)}\right). \tag{1.4}$$

The ratio A_2/A_0 provides a direct measure of bar strength, and the maximum of this radial profile is typically adopted as the global bar strength (e.g., H. Salo et al., 2010). This method is extensively used in both N-body simulations (e.g., Athanassoula and Misiriotis, 2002; Victor P. Debattista, Maria Corsini, and Aguerri, 2002) and observations (e.g., Ohta, Hamabe, and Wakamatsu, 1990; E. Laurikainen, H. Salo, and Rautiainen, 2002; Eija Laurikainen, Heikki Salo, and Ronald Buta, 2004).

1.3.2 Bar Length

The bar length, denoted as $R_{\rm bar}$, measures how far the bar extends across the galactic disc and is one of the most fundamental bar properties. However, estimating it accurately is challenging because bars are continuous structures that gradually blend into the central bulge and surrounding spiral arms (Ghosh and Paola Di Matteo, 2024). Below, a few methods for determining the bar radius ($R_{\rm bar}$), as commonly used in the literature, are described.
– the radial distance over which the phase angle of the $m = 2$ Fourier term (ϕ_2) remains nearly constant, typically within a narrow range of 3°-5°;
– the radius at which the strength of the $m = 2$ Fourier component, expressed as the ratio A_2/A_0, reaches its maximum value;
– the radius where the $m = 2$ Fourier amplitude ratio (A_2/A_0) drops to about 70% of its peak strength;
– the region where the contrast between the bar intensity (I_b) and the inter-bar intensity (I_{ib}) exceeds 2, i.e., $I_b/I_{ib} > 2$;
– the radius defined by the threshold condition applied to the bar-to-inter-bar intensity ratio (I_b/I_{ib}) in this estimator.

$$\frac{I_b}{I_{ib}} > \left(\frac{I_b}{I_{ib}}\right)_{\rm min} + \frac{1}{2}\left[\left(\frac{I_b}{I_{ib}}\right)_{\rm max} - \left(\frac{I_b}{I_{ib}}\right)_{\rm min}\right]. \tag{1.5}$$

The definitions of the bar and interbar intensities used here also follow earlier works, particularly Aguerri, Muñoz-Tuñón, et al. (2000). These intensities are computed from the even Fourier components as

$$I_b(R) = I_0(R) + I_2(R) + I_4(R) + I_6(R), \tag{1.6}$$

and

$$I_{ib}(R) = I_0(R) - I_2(R) + I_4(R) - I_6(R), \tag{1.7}$$

where I_m denotes the amplitude of the mth Fourier mode. These quantities quantify the contrast between the bar and its surrounding disc and form the basis of the intensity-based bar-length estimators.

In the Fourier decomposition method, the bar length is often estimated by locating either the radius where the A_2 amplitude begins to drop sharply or the radius at which the phase angle $\Phi_2(r)$ shows a clear deviation, indicating the transition from the bar-dominated region to the surrounding spiral structure. Bar length and bar strength are generally the most straightforward bar parameters to measure from optical or infrared observations, as they directly trace the bar's stellar light distribution (e.g., Peter Erwin, 2005; Dimitri A. Gadotti, 2011).

1.3.3 Bar pattern speed

The pattern speed, $\Omega_{\rm bar}$, describes the angular frequency with which the bar rotates. It plays a central role in the dynamical structure of galaxies because it determines the locations of resonances such as the corotation resonance ($R_{\rm CR}$) and the Lindblad resonances. A self-consistent bar cannot extend beyond its corotation radius $R_{\rm CR}$, as stellar orbits outside this radius no longer align constructively with the bar's potential. The dimensionless ratio

$$\mathcal{R} = \frac{R_{\rm CR}}{R_{\rm bar}} \tag{1.8}$$

is therefore a key diagnostic of bar dynamics. Bars with $1.0 < \mathcal{R} < 1.4$ are classified as 'fast', whereas $\mathcal{R} > 1.4$ corresponds to 'slow' bars. Values $\mathcal{R} < 1.0$ imply 'ultrafast' bars, which are considered dynamically unlikely (e.g., Victor P. Debattista, Maria Corsini, and Aguerri, 2002; Rautiainen, H. Salo, and E. Laurikainen, 2008).

However, obtaining accurate measurements of these dynamical properties remains challenging. As reported by Ghosh and Paola Di Matteo (2024), one of the major sources of uncertainty arises from the difficulty in robustly determining the bar length, since even a small error in $R_{\rm bar}$ directly propagates into estimates of $\mathcal{R}$. Since $\mathcal{R}$ depends on both the corotation radius and the bar length, such uncertainties can significantly bias the inferred dynamical state of a galaxy when classifying bars as fast or slow. Therefore, a precise determination of the bar pattern speed $\Omega_{\rm bar}$, together with reliable estimates of $R_{\rm bar}$, is essential for understanding bar-driven secular evolution and for constraining the efficiency of dynamical friction exerted by the dark matter halo on the rotating bar (e.g., Victor P. Debattista and J. A. Sellwood, 2000; Athanassoula, 2003; J. A. Sellwood, 2014).

1.4 *Pattern speed measurement of bars & the associated challenges*

Over the past decades, a variety of techniques have been developed to estimate the bar pattern speed, $\Omega_{\rm bar}$. Owing to our internal vantage point, studies of the Milky Way bar benefit from detailed stellar phase-space information, enabling the use of star counts, stellar kinematics, and orbit-based dynamical modelling. In this case, $\Omega_{\rm bar}$ is typically constrained by matching self-consistent dynamical models to observed stellar density distributions and velocity fields, rather than through direct application of methods used for external galaxies (e.g., James Binney et al., 1991; Dehnen, 2000). These approaches provide strong constraints but rely on complex modelling and assumptions about the Galactic potential and bar structure. In contrast, measurements of $\Omega_{\rm bar}$ in external barred galaxies must rely on indirect techniques that infer the pattern speed from projected observables. Early approaches were based on hydrodynamical simulations, in which the gas response to a modelled gravitational potential was compared with observed gas morphology and kinematics, treating $\Omega_{\rm bar}$ as a free parameter adjusted to reproduce features such as shocks, dust lanes, or velocity fields (e.g., Sanders and Tubbs, 1980; Hunter et al., 1988; García-Burillo, F. Combes, and Gerin, 1993; Laine and Heller, 1999; Weiner, J. A. Sellwood, and T. B. Williams, 2001; Rautiainen, H. Salo, and E. Laurikainen, 2008). Although successful in reproducing large-scale gas flows, these methods are inherently model-dependent and sensitive to assumptions about the gas physics and the underlying gravitational potential. Another commonly used class of techniques exploits morphological indicators, such as resonance rings, spiral arm phase changes, or dust-lane geometries, which are assumed to be associated with specific resonances, most commonly corotation (e.g., R. Buta, 1986; Canzian, 1993; Aguerri, Beckman, and Prieto, 1998; R. J. Buta and Zhang, 2009). While these methods provide useful qualitative constraints, they yield only approximate estimates of $\Omega_{\rm bar}$ and depend on uncertain resonance identification.

The most widely used approach to determine the bar pattern speed in external galaxies is the non-parametric method proposed by Tremaine and Weinberg (1984), commonly known as the Tremaine–Weinberg (TW) method. This technique provides a direct, model-independent estimate of $\Omega_{\rm bar}$ using luminosity-weighted integrals of line-of-sight surface brightness and line-of-sight velocity. For a tracer population that obeys the continuity equation, the TW method gives

$$\Omega_{\rm bar} \sin i = \frac{\langle V_{\rm los} \rangle}{\langle X \rangle}, \tag{1.9}$$

where i is the inclination of the galaxy disc, and $\langle V_{\rm los} \rangle$ and $\langle X \rangle$ are luminosity-weighted mean quantities measured along slits or pseudo-slits that are orientated parallel to the observed major axis. Since it does not require an assumed potential, orbit model, or resonance identification, the TW method remains the only fully model-independent technique for bar pattern speed measurements. For a full exposition of this method, see Chapter 2.

Over the past years, the TW method has been successfully applied to many barred galaxies across the Hubble sequence (e.g., Michael R. Merrifield and Konrad Kuijken, 1995; Victor P. Debattista, Maria Corsini, and Aguerri, 2002;

Joris Gerssen, Konrad Kuijken, and Michael R. Merrifield, 2003; Olivier Hernandez et al., 2005; E. M. Corsini, Aguerri, Victor P. Debattista, et al., 2007; Chemin and O. Hernandez, 2009; Aguerri et al., 2015). These applications consistently reveal that most bars in nearby galaxies are 'fast', supporting theoretical expectations that bars in evolved systems undergo relatively weak dynamical friction exerted by the dark matter halo. However, the reliability of these results ultimately depends on how well the assumptions of the TW method are satisfied, motivating the need to examine its performance under realistic non-axisymmetric conditions.

1.5 Formation of lopsidedness and co-existence with bars

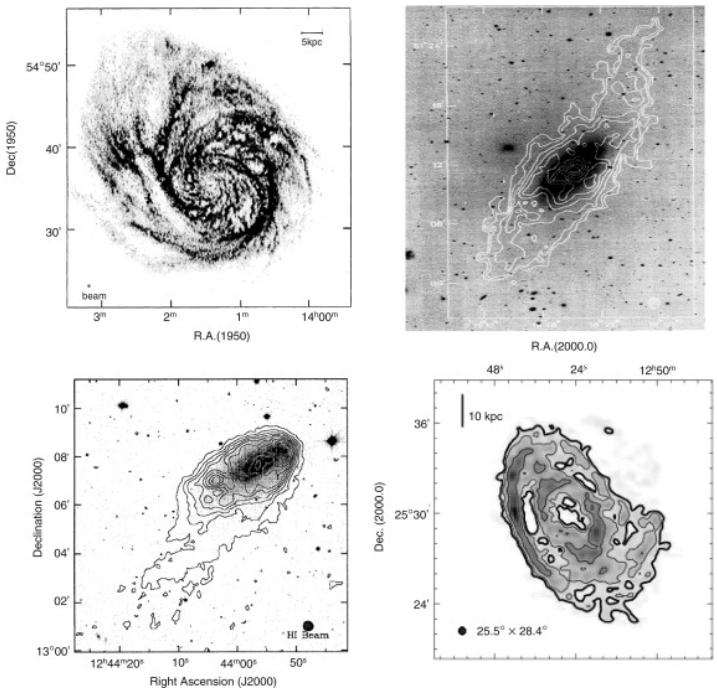


Figure 1.3: *Presence of an $m = 1$ lopsidedness in observed galaxies. Top left panel:* M101 showing a grey-scale map of its lopsided H I intensity (Braun, 1995). *Top right panel:* H I intensity contours overlaid on an optical image of NGC 2841, revealing its lopsided gas disc (Bosma, 1981). *Bottom left panel:* H I contours superimposed on an optical image of NGC 4654, another example of a lopsided disc (Phookun and Mundy, 1995). *Bottom right panel:* Combined contour and grey-scale map of the H I intensity in UGC 7989 (E. Noordermeer et al., 2005).

Many disc galaxies exhibit large-scale $m = 1$ asymmetry, commonly known as *lopsidedness*, which appear as an uneven distribution of mass or light with respect to the galactic centre. This phenomenon has been observed in both the stellar and gaseous components of numerous nearby galaxies (e.g., Baldwin, Lynden-Bell, and Sancisi, 1980; Richter and Sancisi, 1994; Rix and Zaritsky, 1995; Haynes et al., 1998; F. Bournaud et al., 2005; Angiras et al., 2006; Timothy A. Reichard et al., 2008; van Eymeren et al., 2011; Zaritsky, Heikki Salo, et al., 2013). In the neutral hydrogen (H I) component, lopsidedness is especially prominent, where one side of the disc appears more extended or massive compared to the opposite

side. This global $m = 1$ mode was first systematically identified by Baldwin, Lynden-Bell, and Sancisi (1980). These observational signatures are illustrated in Figure 1.3, which presents several well-studied examples of lopsided galaxies in H I. In M101 and NGC 2841 (top panels), the H I distribution clearly shows an asymmetric extension of gas on one side of the disc. The lower panels, showing NGC 4654 and UGC 7989, further highlighting this behaviour, where the outer gas layers are significantly more extended along a preferred azimuthal direction. Together, these systems demonstrate that $m = 1$ asymmetries are common and easily identifiable, especially in the outer H I discs of nearby galaxies.

The Milky Way itself displays measurable lopsidedness both in the H I gas (Kalberla and Dedes, 2008) and the stellar disc (Romero-Gómez et al., 2019). Lopsidedness often manifests not only as a morphological asymmetry but also through kinematic signatures, such as an offset in the velocity field relative to the photometric centre (Schoenmakers, Franx, and de Zeeuw, 1997; Swaters et al., 1999). In Fourier analysis, the $m = 1$ amplitude quantifies the strength of this distortion and is often measured as the ratio A_1/A_0. Observations typically report values in the range $0.1 \lesssim A_1/A_0 \lesssim 0.3$, suggesting that mild lopsidedness is widespread in disc galaxies (Zaritsky and Rix, 1997; Rix and Zaritsky, 1995; Jog and Francoise Combes, 2009).

Lopsidedness can arise from several external and internal mechanisms. External processes such as tidal interactions, minor mergers, and asymmetric gas accretion can excite a long-lived $m = 1$ mode in a galactic disc (e.g., Rix and Zaritsky, 1995; F. Bournaud et al., 2005; Mapelli, Moore, and Bland-Hawthorn, 2008; Ghosh, Kanak Saha, Jog, et al., 2022). These mechanisms tend to concentrate mass along a preferred azimuthal direction, producing an off-centred, one-sided appearance. Internal processes may also sustain lopsidedness: for example, a displacement between the centres of the stellar disc and the dark matter halo can generate a persistent $m = 1$ mode (e.g., Edo Noordermeer, Sparke, and Levine, 2001; Kanak Saha, Francoise Combes, and Jog, 2007; Prasad and Jog, 2017). Numerical simulations further show that lopsidedness can survive for several gigayears, especially in galaxies with dynamically cold outer discs (Ghosh, Kanak Saha, Jog, et al., 2022).

More importantly, lopsidedness is frequently observed to coexist with stellar bars, indicating that $m = 1$ and $m = 2$ modes are not mutually exclusive. Observational studies show that a significant fraction of barred galaxies exhibit measurable lopsidedness in either their stellar or gaseous components (e.g., Rix and Zaritsky, 1995; F. Bournaud et al., 2005; Timothy A. Reichard et al., 2008). This coexistence suggests that the presence of a bar does not necessarily suppress $m = 1$ asymmetries and that both modes can be simultaneously sustained over long timescales. From a dynamical perspective, the bar ($m = 2$) and lopsided ($m = 1$) modes generally rotate with different pattern speeds. The $m = 1$ mode is typically slow and, in some cases, may even rotate retrograde relative to the bar (Ghosh, Soumavo et al., 2023; Jog and Francoise Combes, 2009). This difference in pattern speeds allows the two modes to coexist without rapidly destroying each other. Numerical simulations demonstrate that bars can survive in lopsided discs and, in some cases, may even enhance or maintain the $m = 1$ asymmetry through non-linear mode coupling (Athanassoula, 2003; Ghosh, Kanak Saha, Jog, et al., 2022). The simultaneous presence of $m = 1$ and $m = 2$

modes leads to a complex dynamical environment in which resonances associated with both patterns may overlap. Such resonance overlap can influence angular momentum redistribution, gas inflow, and secular evolution of the disc (J. A. Sellwood, 2014; Ghosh, Soumavo et al., 2023). As a result, the coexistence of bars and lopsidedness plays an important role in shaping the long-term structural and dynamical evolution of disc galaxies.

1.6 Scientific goal of the thesis

The Tremaine–Weinberg (TW) method is one of the most widely used techniques for measuring the pattern speeds of bars in disc galaxies. However, it relies on several key assumptions that are often difficult to satisfy in real systems. First, the tracer population must obey the continuity equation, implying negligible ongoing star formation, dust obscuration, or strong radial flows. Secondly, the method assumes that the pattern under study rotates as a single rigid structure with a well-defined pattern speed. Finally, and most critically, the TW method requires the underlying disc to be perfectly axisymmetric outside the bar region. Under this assumption, any luminosity or velocity asymmetry measured along symmetrically placed slits is attributed solely to the bar.

In practice, real galaxies frequently violate these ideal conditions. Structures such as spiral arms, warps, dust lanes, or an $m = 1$ large-scale lopsidedness introduce non-axisymmetric distributions of light and velocity that contaminate the luminosity-weighted integrals used in the TW calculation. Even relatively weak asymmetries can shift the luminosity centroid or distort the $\langle V_{\rm los} \rangle$ integrals, leading to biased estimates of the bar pattern speed, $\Omega_{\rm bar}$. Although the TW method has been extensively applied, most previous studies implicitly assume that disc galaxies are close to axisymmetric apart from the bar itself. At the same time, both observations and simulations show that a substantial fraction of disc galaxies exhibit significant large-scale an $m = 1$ lopsidedness, commonly induced by minor mergers or tidal interactions. The impact of such disc asymmetries on TW-based measurements of bar pattern speeds has not yet been systematically investigated, leaving a clear gap in the existing literature.

This thesis is designed to address this gap by exploring the interplay between two fundamental aspects of galaxy dynamics: bar pattern speed measurements and disc lopsidedness. The primary goal of this work is to quantify how an $m = 1$ lopsidedness affects the measurement of $\Omega_{\rm bar}$ and to assess the robustness of the TW method when the assumption of axisymmetry is violated.

To achieve this, we use the publicly available GalMer database of N-body+SPH simulations (Chilingarian et al., 2010), which provides a diverse set of minor merger models spanning a range of orbital parameters and galaxy morphologies. We focus on systems in which minor mergers generate strong $m = 1$ lopsidedness disc asymmetries and analyse the resulting dynamical coupling between bars and lopsidedness.

The novelty of this study lies in providing the first direct, simulation-based test of the TW method in the presence of strong $m = 1$ lopsidedness, where the true bar pattern speed is independently known. By quantifying the systematic biases introduced by such asymmetries, this work offers critical guidance for interpreting observational measurements of $\Omega_{\rm bar}$ in lopsided barred galaxies.

More generally, the results will help refine the applicability and limitations of the TW technique, contributing to more reliable dynamical studies of barred galaxy evolution in realistic environments.

Chapter 2

The Tremaine-Weinberg Method

The Tremaine-Weinberg (TW) method (Tremaine and Weinberg, 1984) is one of the most important techniques in galactic dynamics because it provides the only fully model-independent measurement of the pattern speed of bars in disc galaxies. Unlike hydrodynamical modelling (Weiner, J. A. Sellwood, and T. B. Williams, 2001; Rautiainen, H. Salo, and E. Laurikainen, 2008), morphological indicators (R. J. Buta and Zhang, 2009), or resonance-based methods (Canzian, 1993), the TW method derives the pattern speed directly from observational data without requiring any assumptions about the gravitational potential, gas equation of state, or orbital structure. Its original and simplest implementation uses long-slit spectroscopic observations and relies solely on the continuity equation for a tracer population, along with the assumption that the bar rotates rigidly with a single angular frequency. Due to its simplicity and reliability, the TW method has become a standard tool for measuring bar pattern speed in external galaxies.

Modern Integral Field Unit (IFU) observations provide full three-dimensional kinematic information and enable the selection of large, 2D samples of barred galaxies spanning a wide range of morphologies. Publicly available surveys such as the Mapping Nearby Galaxies at Apache Point Observatory (MaNGA; Bundy et al. 2015), the Calar Alto Legacy Integral-field Spectroscopy Area Survey (CALIFA; Sánchez, R. C. Kennicutt, Gil de Paz, et al. 2012), and the Sydney–Australian Astronomical Observatory Multi-object Integral-field Spectrograph survey (SAMI; Croom et al. 2012) have significantly enhanced the application of the Tremaine–Weinberg (TW) method. IFU data allow the construction of multiple pseudo-slits from a single observation, improving robustness and reducing systematic uncertainties related to slit placement and disc position-angle errors (Victor P. Debattista, 2003). The TW method has been widely applied to real galaxies using both long-slit and integral-field spectroscopy. Early stellar long-slit studies provided the first direct measurements of bar pattern speeds in nearby galaxies and established that most bars rotate rapidly (Kent, 1986; Michael R. Merrifield and Konrad Kuijken, 1995; J. Gerssen, K. Kuijken, and M. R. Merrifield, 1999; Joris Gerssen, Konrad Kuijken, and Michael R. Merrifield, 2003; E. M. Corsini, Aguerri, and V. P. Debattista, 2003; E. M. Corsini, Aguerri, Victor P. Debattista, et al., 2007). With the advent of integral-field spectroscopy, the method has been extended to larger and more diverse samples. CALIFA-based studies demonstrated the feasibility of applying the TW method to late-type and low surface-brightness galaxies (Enrico M. Corsini, 2011; Aguerri et al., 2015). In addition to stellar tracers, the TW method has also been applied using gaseous components in selected systems, although such measurements are more sensitive to shocks and non-steady-state effects (Borodina, Thomas G. Williams, et al., 2023b).

2.1 Formulation of the TW method

The foundation of the TW method is that the tracer population obeys the continuity equation as follows,

$$\frac{\partial \Sigma}{\partial t} + \nabla \cdot (\Sigma \mathbf{u}) = 0, \tag{2.1}$$

which expresses conservation of mass (or luminosity) for a tracer population. Here, $\Sigma(x, y, t)$ is the surface density and $\mathbf{u}(x, y, t)$ is the planar velocity field of the tracer population. If a non-axisymmetric pattern such as a bar rotates rigidly with pattern speed $\Omega_{\rm bar}$, the surface density must satisfy

$$\Sigma(R, \phi, t) = \Sigma(R, \phi - \Omega_{\rm bar} t), \tag{2.2}$$

and therefore

$$\frac{\partial \Sigma}{\partial t} = -\Omega_{\rm bar} \frac{\partial \Sigma}{\partial \phi}. \tag{2.3}$$

To illustrate how this leads to the TW relation, we expand the azimuthal derivative in Cartesian coordinates using the identity

$$\frac{\partial}{\partial \phi} = -y \, \frac{\partial}{\partial x} + x \, \frac{\partial}{\partial y}. \tag{2.4}$$

Substituting this into the time derivative gives

$$\frac{\partial \Sigma}{\partial t} = \Omega_{\rm bar} \left(y \frac{\partial \Sigma}{\partial x} - x \frac{\partial \Sigma}{\partial y} \right). \tag{2.5}$$

Replacing $\partial \Sigma / \partial t$ in the continuity equation and regrouping terms yields

$$\frac{\partial}{\partial x} \left[\Sigma \left(u_x + \Omega_{\rm bar} y \right) \right] + \frac{\partial}{\partial y} \left[\Sigma \left(u_y - \Omega_{\rm bar} x \right) \right] = 0. \tag{2.6}$$

Integrating equation (2.6) over x from $-\infty$ to $+\infty$ and assuming that $\Sigma \to 0$ at large radii (so that boundary terms vanish), we obtain

$$\frac{d}{dY} \int_{-\infty}^{+\infty} \Sigma \left(u_y - \Omega_{\rm bar} X \right) \, dX = 0. \tag{2.7}$$

Multiplying by an arbitrary weighting function $h(Y)$ and integrating over Y leads to

$$\Omega_{\rm bar} \int h(Y) \int X \, \Sigma \, dX \, dY = \int h(Y) \int \Sigma \, u_y \, dX \, dY. \tag{2.8}$$

To relate the right-hand side to observables, we project the in-plane velocity along the line of sight. For a thin disc, the observed line-of-sight velocity is

$$V_{\rm los}(X, Y) - V_{\rm sys} = u_y(X, Y) \, \sin i. \tag{2.9}$$

Substituting this projection into the previous integral yields the Tremaine-Weinberg relation:

$$\Omega_{\rm bar} \sin i = \frac{\int h(Y) \int \Sigma(X,Y) [V_{\rm los}(X,Y) - V_{\rm sys}] \, dX \, dY}{\int h(Y) \int [X - X_{\rm c}] \, \Sigma(X,Y) \, dX \, dY}, \tag{2.10}$$

where (X, Y) are sky-plane coordinates aligned with the projected major and minor axes, i is the inclination, $X_{\rm c}$ is the adopted photometric centre, and $h(Y)$ selects individual slits or pseudo-slits. This expression forms the classic TW equation (Tremaine and Weinberg, 1984), which is later rewritten into its observationally practical form using luminosity-weighted mean quantities (Michael R. Merrifield and Konrad Kuijken, 1995). Merrifield and Kuijken reformulated this expression to improve signal-to-noise by collapsing each slit into luminosity-weighted mean quantities. They defined the luminosity-weighted velocity and position as

$$\langle V_{\rm los} \rangle = \frac{\int V_{\rm los}(X,Y) \, \Sigma(X,Y) \, dX}{\int \Sigma(X,Y) \, dX}, \tag{2.11}$$

$$\langle X \rangle = \frac{\int X \, \Sigma(X,Y) \, dX}{\int \Sigma(X,Y) \, dX}. \tag{2.12}$$

Under these definitions, the pattern speed is the slope of the relation between $\langle V_{\rm los} \rangle$ and $\langle X \rangle$:

$$\Omega_{\rm bar} \sin i = \frac{\langle V_{\rm los} \rangle - V_{\rm sys}}{\langle X \rangle - X_{\rm c}}. \tag{2.13}$$

This linear form is used in almost all modern long-slit and integral-field applications of the method, both in long-slit spectroscopic studies of individual barred galaxies (e.g., Michael R. Merrifield and Konrad Kuijken, 1995; Aguerri, Victor P. Debattista, and Maria Corsini, 2003; Olivier Hernandez et al., 2005) and in large IFU survey analyses such as MaNGA and CALIFA (e.g., Garma-Oehmichen et al., 2019; Zou et al., 2019; Cuomo, Virginia et al., 2021; Lee et al., 2022), using pseudo-slit extractions.

2.2 *Assumptions of the TW method*

The TW method, although elegant, depends on three vital assumptions. The first one is that the tracer population must obey the continuity equation. This condition is best satisfied by old stellar populations whose surface brightness evolves slowly and is not strongly affected by patchy star formation, shocks, or dust extinction (Michael R. Merrifield and Konrad Kuijken, 1995; Victor P. Debattista, Maria Corsini, and Aguerri, 2002; Enrico M. Corsini, 2011). Gas tracers, especially H I and Hα, often violate continuity due to shocks, inflows, and variable emission-line strengths (Rand, 1995; Olivier Hernandez et al., 2005; Fathi et al., 2009; Borodina, Thomas G Williams, et al., 2023a).

A second assumption is that the bar rotates as a rigid pattern with a single constant angular frequency. Observationally, galaxies may host multiple pattern

speeds from nuclear spirals (P. Erwin, 2011), outer spirals (Meidt et al., 2009), and $m = 1$ asymmetries (T. A. Reichard et al., 2008; Zaritsky, Heikki Salo, et al., 2013). If these structures significantly contribute to the light or velocity fields in the region used by the TW integrals, they distort the linear relation and bias the measurement.

The third key assumption is that the disc underlying perfectly axisymmetric. This ensures that the luminosity-weighted integrals are dominated by the bar alone. Other disc asymmetries such as lopsidedness (Baldwin, Lynden-Bell, and Sancisi, 1980; Zaritsky, Heikki Salo, et al., 2013), strong spiral arms (Victor P. Debattista, Mayer, et al., 2006), or warps (K. Saha, Jong, and Holwerda, 2009) shift the centroids of $\langle X \rangle$ and $\langle V_{\rm los} \rangle$, changing the inferred slope of the Tremaine-Weinberg relation.

2.3 *Sources of Error and Uncertainties*

The reliability of pattern-speed measurements obtained through the Tremaine-Weinberg (TW) method is strongly influenced by both geometric and observational factors. Among these, the orientation of the galaxy, slit configuration, and instrumental limitations play dominant roles in shaping the final uncertainty budget.

2.3.1 *Galaxy Inclination Effects*

Galaxy inclination is a primary determinant of the quality of TW measurements. Nearly face-on systems yield very small line-of-sight velocities, leading to noisy and unstable TW relations (Victor P. Debattista, Maria Corsini, and Aguerri, 2002). Conversely, highly inclined or edge-on galaxies suffer from severe projection effects, dust obscuration, and loss of reliable photometric information. Observational studies consistently indicate that intermediate inclinations, typically in the range $15^\circ \lesssim i \lesssim 70^\circ$, provide the most robust TW measurements (Garma-Oehmichen et al., 2019). Inclination uncertainties also propagate directly into the deprojection factor through $\sin i$, introducing systematic errors in the derived pattern speed.

2.3.2 *Bar Orientation Relative to the Disc*

The orientation of the bar with respect to the disc major axis critically affects the strength of the TW signal. When the bar is aligned close to either the major or minor axis, the luminosity-weighted mean position varies weakly across the slits, reducing the sensitivity of the TW relation. Bars observed at intermediate, oblique angles relative to the major axis produce stronger and more stable correlations between $\langle V_{\rm los} \rangle$ and $\langle X \rangle$, resulting in more reliable pattern-speed estimates (Zou et al., 2019).

2.3.3 *Slit Placement*

Slit configuration introduces additional sources of uncertainty. Each slit must adequately sample the full extent of the bar to capture the non-axisymmetric signal

that underpins the TW method. Slits that are too short fail to encompass the bar, while those extending too far into the outer disc risk contamination from spiral arms or other asymmetries, violating the assumptions of the method. Empirical tests suggest that slit lengths of approximately 1.2 $R_{\rm bar}$ offer an optimal balance between bar coverage and minimisation of contamination (Garma-Oehmichen et al., 2019).

2.3.4 *Disc Position Angle*

Among all observational parameters, the disc position angle (PA) represents the most critical source of systematic uncertainty. Even a small PA error of a few degrees can induce errors of 40-50% in the derived pattern speed (Victor P. Debattista and T. B. Williams, 2004; Garma-Oehmichen et al., 2019). Accurate determination of the disc geometry through careful photometric decomposition is therefore essential for reliable TW measurements.

2.3.5 *Galaxy Centre Determination*

Uncertainties in identifying the galaxy centre further contribute to systematic errors. Photometric and kinematic centres may not coincide, particularly in galaxies affected by dust lanes, lopsidedness, or non-axisymmetric structures (E. M. Corsini, Aguerri, Victor P. Debattista, et al., 2007). Miscentring alters the luminosity-weighted integrals and can bias the resulting TW slope.

2.3.6 *Instrumental and Observational Limitations*

Instrumental effects such as limited spatial resolution, low signal-to-noise ratios in velocity measurements, and patchy dust extinction introduce additional scatter in the TW integrals. While integral-field spectroscopy offers complete two-dimensional kinematic coverage, it also reveals irregular velocity structures in late-type galaxies that may violate the continuity assumptions of the TW method (Aguerri et al., 2015; Garma-Oehmichen et al., 2019).

2.3.7 *Effects of Noise and Non-Axisymmetric Structures*

Random noise in velocity or surface-brightness maps introduces scatter in the $\langle V_{\rm los}\rangle$–$\langle X\rangle$ relation but usually contributes less to the total uncertainty than geometric misalignments. However, contamination from spiral arms, warps, or lopsided structures can bias TW measurements if they significantly affect the luminosity-weighted integrals. Such effects must be carefully assessed, particularly when applying the TW method to late-type or dynamically disturbed discs.

Chapter 3

The GaLMer database

2

The GalMer database (Chilingarian et al., 2010) is a public library of *N*-body+SPH (smoothed particle hydrodynamics) simulations to model the evolution of galaxy formation through the hierarchical merger process. It explores a wide variety of initial conditions (see Table 4.1), including galactic morphologies, gas fractions, orbital configurations (see Figure 3.1), and mass ratios. Each system is initialised in dynamical equilibrium, accounting for gravity, gas dynamics, and star formation. These configurations enable the study of how varying geometry, inclination, and orbital energy influence tidal features and angular momentum exchange during galaxy interactions.

The GalMer simulations have been extensively used in a wide range of follow-up studies to investigate the dynamical and structural consequences of galaxy interactions. For example, P. Di Matteo et al. (2007) used GalMer simulations to study the efficiency of gas inflow and star formation enhancement during galaxy mergers as a function of orbital parameters. Montuori et al. (2010) employed GalMer models to examine the evolution of gas metallicity gradients induced by tidal interactions and mergers. The impact of mergers on disc survival and kinematic misalignments was explored using GalMer simulations by Randriamampandry et al. (2016).

More recent studies have made extensive use of the GalMer database. Prakash, Banerjee, and Perepu (2020) used images from the GalMer N-body + SPH simulations of 1:1 mergers of interacting galaxy pairs at their pericentric approach to train deep convolutional neural network (DCNN) models, while Mahor et al. (2021) analysed the generation of tidal features and stellar streams resulting from unequal-mass interactions. The GalMer simulations were further employed by Ghosh, Kanak Saha, Di Matteo, et al. (2021) to investigate the dynamical impact of minor galaxy mergers on the survival of stellar bars. Their study explored a range of parameters, including orbital energy, orientation of the orbital spin vector, and the morphology of the satellite galaxy, using the GalMer library of galaxy-merger simulations to examine the temporal evolution of bar properties before and after the merger. Additionally, Ghosh, Kanak Saha, Jog, et al. (2022) investigated the dynamical impact of minor mergers (mass ratio 1:10) on the excitation of an $m = 1$ lopsided distortion in the stellar density and velocity fields.

3.1 Equilibrium Galaxy Model

All galaxy models in GalMer are constructed to represent dynamically stable, isolated systems before interaction. The GalMer database provides simulations covering the full Hubble sequence with five different galaxy morphologies, namely E0 ellipticals, S0 lenticulars, and Sa–Sd spirals, where each galaxy is also categorised by its mass as either giant (g), intermediate (i), or dwarf (d). The merger scenarios are accordingly denoted as the giant-dwarf minor merger (mass

ratio of 1:10), the giant-intermediate merger (mass ratio of 1:2), and the giant-giant major merger (mass ratio of 1:1), representing interaction between host and satellite galaxies. Each galaxy model is initialised in a state of dynamical equilibrium, with gravitational, centrifugal, and pressure forces among the dark matter halo, a stellar disc, a gaseous disc (when included), and a central bulge. The dark matter halo and the bulge are represented by Plummer density profiles (Plummer, 1911) given as

$$\rho(r) = \frac{3M}{4\pi a^3}\left(1 + \frac{r^2}{a^2}\right)^{-5/2} \tag{3.1}$$

Where M is the total mass, r is the distance from the centre, and a is the scale length. The stellar and gaseous discs are described by Miyamoto–Nagai profiles (Miyamoto and Nagai, 1975) in eq. (3.2) in cylindrical coordinates, whose density has the following form

$$\rho(R,z) = \frac{Mb^2}{4\pi}\frac{aR^2 + (a+3\zeta)(a+\zeta)^2}{\zeta^3[R^2 + (a+\zeta)^2]^{5/2}}, \tag{3.2}$$

where $\zeta = \sqrt{z^2 + b^2}$, M is the total mass, a and b are the parameters which controls the radial and vertical extents of the disc, respectively.

The stellar disc mass ranges from $9.2 \times 10^{10}\, M_\odot$ in early-type galaxies such as gS0 and gSa, $5.8 \times 10^{10}\, M_\odot$ in late-type systems like gSd. The bulge mass decreases from $M_B = 1.6{\times}10^{11} M_\odot$ for gE0 to $M_B = 0$ for gSd, while the gas mass increases from $M_g = 9.2 \times 10^9 M_\odot$ in gSa to $1.7 \times 10^{10} M_\odot$ in gSd. The Toomre stability parameters are fixed at $Q_* = 1.2$ for the stellar disc and $Q_{\rm gas} = 0.3$–1.2 for the gaseous disc to ensure local stability. The typical number of particles used for giant galaxies is $N_{\rm TOT} = 1.2 \times 10^5$, distributed among dark matter, stellar, and gaseous components according to their mass fractions. For intermediate and dwarf galaxies, the particle numbers are scaled to $N_{\rm TOT} = 2.4 \times 10^5$ and $4.8{\times}10^4$, respectively. In addition to the collisionless components, the evolution of the gaseous component is modelled using simplified prescriptions for radiative cooling, star formation, and stellar feedback, consistent with the idealised nature of the GalMer simulations. Star formation follows a Schmidt-type law, whereby gas above a density threshold is converted into stars at a rate dependent on the local gas density (Schmidt, 1959; Robert C. Kennicutt Jr., 1998). Feedback associated with star formation is treated in a parameterised manner, regulating gas consumption during the interaction and merger phases (P. Di Matteo et al., 2007).

3.2 Orbital Parameters

The orientation of each galaxy within the orbital plane is defined by the spherical angles i_1, i_2, Φ_1, and Φ_2 (see Fig. 3.1). These parameters are varied alongside the initial orbital energy (E) and angular momentum (L) to explore both prograde (direct) and retrograde orbital configurations.

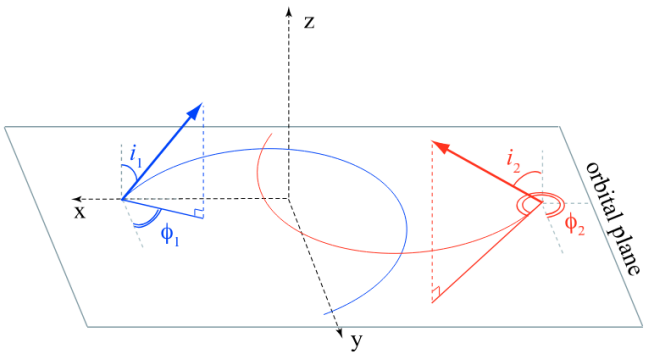


Figure 3.1: Orbital configuration implemented in the GalMer simulations, taken from Chilingarian et al. (2010). The collision is initialised with the total orbital angular momentum aligned along the z-axis, and the galactic centres positioned on the x-axis at the start. The intrinsic angular momenta (spins) of the two galaxies are indicated by the blue and red arrows, parameterised by the spherical angles (i_1, Φ_1) and (i_2, Φ_2), respectively.

The initial positions and velocities are defined such that the orbital angular momentum vector aligns with the z-axis, while both galaxies lie initially along the x-axis. For giant–dwarf galaxy encounters, a more general setup is adopted with $i_1 = 33°$ and $i_2 = 130°$ representing orientations between halo spin and orbital planes. This is justified geometrically, since the probability of a random spin orientation follows a distribution proportional to $(1 - \cos i_2)$ (Khochfar and Burkert, 2006). Consequently, an orientation between 45° and 90° is about 2.3 times more likely than one between 0° and 45°. The adopted impact parameter, $b = 100$ kpc ($\approx 33 R_d$), lies within the most probable range of 93–127 kpc for a gSa host galaxy of total mass $M = 2.3 \times 10^{11} M_\odot$ and virial radius $r_{200} = 127$ kpc (refer to Table 1). The orbits are typically parabolic or mildly hyperbolic ($E \gtrsim 0$), with the relative velocity chosen to ensure that dynamical friction results in eventual merger within a few Gyrs (for further details, see Chilingarian et al., 2010). Both prograde and retrograde configurations are included to examine the dependence of tidal features and angular momentum transfer on orbital geometry.

3.3 Temporal Evolution

The temporal evolution is computed using a TreeSPH code by Semelin and F. Combes (2002), which combines a hierarchical tree method for gravity (Barnes and Piet Hut, 1986) with smoothed particle hydrodynamics for gas dynamics. For the gravitational force calculation, the code employs a tree algorithm with tolerance parameter $\theta = 0.7$ and includes terms up to quadrupole order in the multipole expansion. Gravitational forces are softened using a Plummer potential, with the softening length set to $\epsilon = 200$ pc for giant-intermediate and giant-dwarf merger models, and $\epsilon = 280$ pc for giant-giant merger models. The equations of motion are integrated using a fixed time-step leapfrog scheme with $\Delta t = 5 \times 10^5$ yr (P. Di Matteo et al., 2007), which is symplectic and time-reversible, ensuring good conservation of energy and angular momentum over long simulation times (Hernquist and Katz, 1989; Springel, 2005). In the GalMer simulations, this integration scheme allows the system to be evolved effi-

ciently over several gigayears while maintaining numerical stability during close encounters and strong tidal interactions. Before the merger simulations begin, all galaxy models are first evolved in isolation for 1 Gyr to ensure stability (Chilingarian et al., 2010). The chosen gravitational softening length and SPH smoothing lengths provide sufficient spatial resolution to resolve internal disc structures, bars, and tidal features throughout the simulation. The merger models follow the GalMer naming convention, as `[host galaxy][satellite galaxy][orbit ID][orbital spin]33`, where `[host galaxy]` and `[satellite galaxy]` indicate the morphological types, `[orbit ID]` corresponds to the orbit number defined in the GalMer database, and `[orbital spin]` specifies the orbital orientation ('dir' for direct and 'ret' for retrograde). The suffix '33' denotes a constant inclination $i_1 = 33°$ used in all minor mergers and then evolves over approximately 3 Gyr, encompassing the stages of first encounter, pericentric passage, tidal stripping, and final coalescence; see Table 4.1. These models are employed to examine the dynamical evolution of the host disc, focusing on angular momentum redistribution and variations in bar pattern speed induced by the merger-driven perturbations.

Chapter 4

Results

4.1 Characterisation of selected minor merger models

In this study, we analyse a set of giant–dwarf minor merger simulations with a 1:10 mass ratio, considering both direct and retrograde orbital configurations. The host galaxy is of Sa type, while the satellite is an E-type system; the corresponding models are denoted as `gSadE006ret33` and `gSadE001dir33`. The initial conditions are based on the standard GalMer setup, adopting $i_1 = 33°$, $i_2 = 130°$, an impact parameter of $b = 100$ kpc and a relative velocity consistent with a marginally bound orbit ($E_{\rm ini} \gtrsim 0$) (more detail in Table 4.1). From the GalMer library, we computed 2-D density-weighted maps for both models (dir and retro), showing the interaction between the host and its companion satellite with two different orbit configurations: one is direct and the other is retrograde, as shown in Figure 4.1. Before initiating the merger process, the galaxy models are evolved for 1 Gyr in isolation, after which the satellite begins its approach relative to the host galaxy disc rotation, either aligned with or opposite to it.

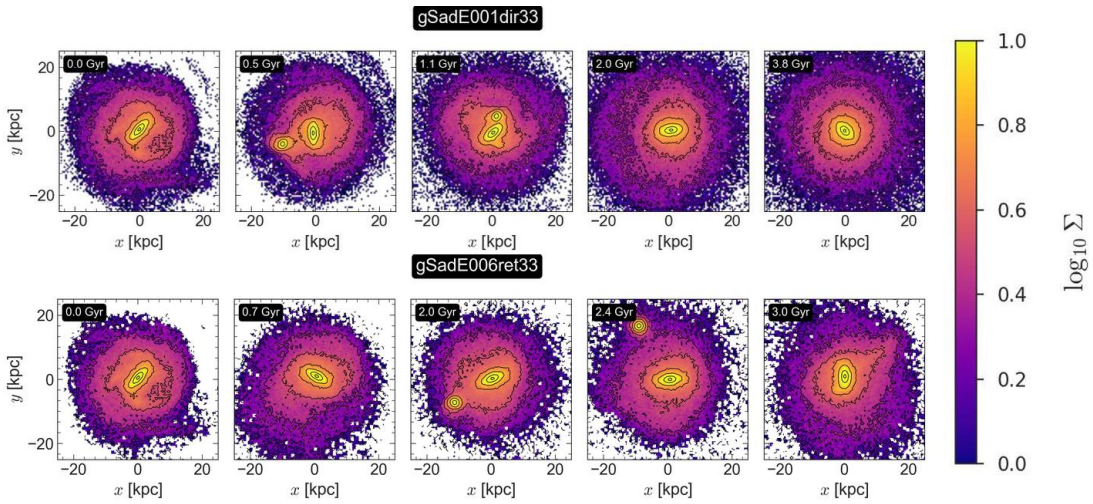


Figure 4.1: Face-on stellar surface-density maps of the combined host (gSa) and satellite (dE0) system are shown at various evolutionary stages for the two minor-merger models, 'gSadE001dir33' (*top panels*) and 'gSadE006ret33' (*bottom panels*). Black lines mark contours of equal surface density, while the colour bar represents the stellar surface density (arbitrary units) for each of the two models.

4.1.1 Orbital separation over time

Figure 4.2 shows the distance between the host and satellite galaxies over time for the two minor-merger models. This separation between the host and satellite is computed by first determining their centres at each time step using density-weighted positions, as tidal tails formed during the interaction can shift the centre of mass, while density-weighted centres better trace the dense central regions.

Table 4.1: Key parameters of the selected GalMer minor-merger models (Chilingarian et al., 2010).

model[(1)]	$r_{\rm ini}^{(2)}$ (kpc)	$V_{\rm ini}^{(3)}$ (10^2 km s^{-1})	$L_{\rm ini}^{(4)}$ (10^3 km s^{-1} kpc)	$E_{\rm ini}^{(5)}$ (10^4 km^2 s^{-2})	spin[(6)]	pericenter[(7)] dist. (kpc)	$T_{1,per}^{(8)}$ (Gyr)	$T_{2,per}^{(9)}$ (Gyr)	$T_{\rm merg}^{(10)}$ (Gyr)	$T_{\rm end}^{(11)}$ (Gyr)
gSadE001dir33	100	1.48	29.66	0.05	up	8.	0.5	1.1	1.55	3.8
gSadE006ret33	100	1.55	36.34	0.1	down	8.	0.45	1.25	1.95	2.85

Notes. Column (1): Model name. Col. (2): Initial separation. Col. (3): Initial velocity. Col. (4): Initial angular momentum. Col. (5): Initial energy. Col. (6): Spin orientation. Col. (7): Pericentre distance. Col. (8): Time of first pericentric passage. Col. (9): Time of second pericentric passage. Col. (10): Merger time. Col. (11): End time of the simulation.

The density-weighted centre is calculated as

$$\mathbf{x}_j = \frac{\sum_i \mathbf{x}_i \, \rho_j^{(i)}}{\sum_i \rho_j^{(i)}}, \tag{4.1}$$

where $\rho_j^{(i)}$ is the local density around the ith particle and $\mathbf{x}_i$ is its position. The density is estimated using

$$\rho_j = \frac{j-1}{V(r_j)}\, m, \tag{4.2}$$

where m is the particle mass and r_j is the distance to the jth nearest neighbour. Here, we choose $j = 6$, as prescribed by Casertano and P. Hut (1985). The three-dimensional distance between the two centres is then used as the orbital separation. Also, 4.1 shows the density-weighted centres of the dark matter halo and stellar disc of the host galaxy at different times.

Both simulations begin with the satellite located nearly 100 kpc from the host, after which the two galaxies move closer under mutual gravity. The curves in Figure 4.2 display a series of dips, each marking a pericentric passage when the satellite makes its closest approach. The difference between the two models becomes evident very quickly. In the direct encounter (red curve), the decay in separation is noticeably faster, and the spacing between pericentres shortens with time. This behaviour resembles observed prograde interactions, where material in the disc and the orbit move in the same direction. In such configurations, the satellite can efficiently transfer its orbital angular momentum to the rotating disc through resonant gravitational interactions. This enhanced coupling strengthens dynamical friction, causing the satellite to lose energy more rapidly and spiral inward at a faster rate, ultimately merging with the host around $t \approx 1.4$ Gyr.

The retrograde model (blue curve) shows a much slower decline in separation, maintaining larger distances for a longer fraction of the simulation. In this case, the orbital motion of the satellite is opposite to the rotation of the host disc, breaking the resonance that normally facilitates angular-momentum transfer. With fewer disc particles moving in the same sense as the satellite's orbit, the gravitational wake is weaker and dynamical friction is significantly reduced. The satellite therefore loses orbital energy more slowly, resulting in later pericentric passages and a delayed final coalescence. This behaviour is consistent with

observational studies of retrograde interactions, which often show extended, long-lived orbits before merging.

Overall, the separation curves in Figure 4.2 reflect the strong connection between orbital geometry and merger efficiency: direct (prograde) encounters decay quickly due to efficient angular-momentum transfer, whereas retrograde encounters decay slowly because this transfer is suppressed, allowing the companion to survive at larger distances for a longer time.

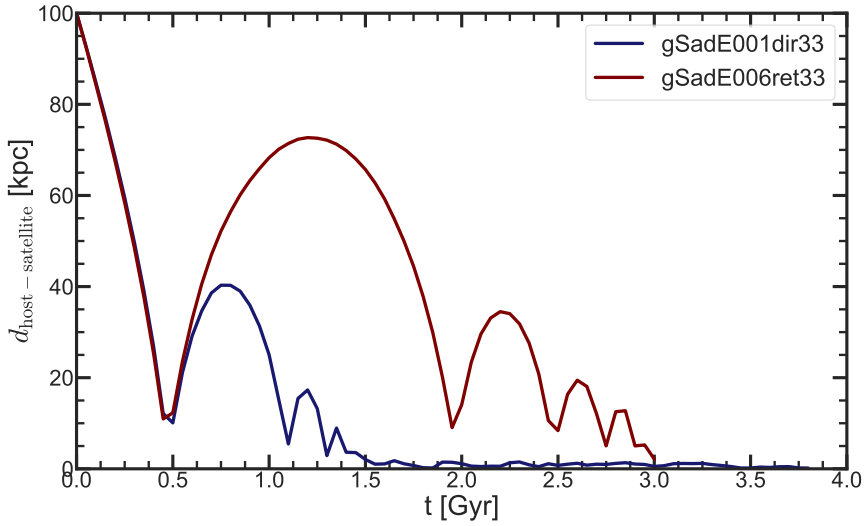


Figure 4.2: *Time evolution of orbital separation between the host and satellite:* The separation (in kpc) between the centres of the satellite (*dE0*) and the host galaxy (*gSa*) is shown as a function of time for the two minor merger models *gSadE001dir33* (in red) and *gSadE006ret33* (in blue). The curves trace the orbital decay, with successive dips indicating pericentric passages and the gradual decrease in separation as the merger progresses.

4.2 Quantification of m=2 bar and m=1 lopsidedness

To characterise the non-axisymmetric structure of the disc, we compute the radial profiles of the Fourier amplitudes for $m = 2$ (bar) and $m = 1$ (lopsided) modes. The Fourier amplitude at a given radius is calculated using the mass distribution from the Fourier decomposition (for more details, see Ghosh, Fragkoudi, et al. (2024)) as

$$A_m/A_0(R) = \left| \frac{\sum_i m_i e^{im\phi_i}}{\sum_i m_i} \right|, \tag{4.3}$$

where ϕ_i is the azimuthal angle for the mass m_i of the ith particle. The amplitudes are normalised by the monopole term A_0, giving $A_m(R)/A_0(R)$ as a function of radius. The resulting radial profiles, presented in Figure 4.3, illustrate how the strength and radial extent of the $m = 1$ and $m = 2$ modes evolve with time during the merger.

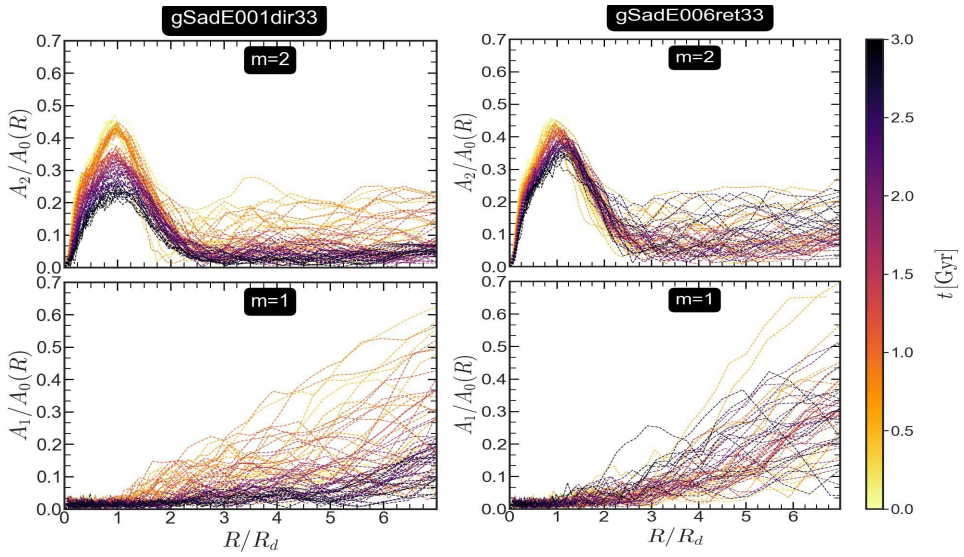


Figure 4.3: Radial profiles of the $m = 2$ and $m = 1$ Fourier coefficients (each normalised by the $m = 0$ component), calculated using Eq. 1.3, are shown as a function of time in Gyr (indicated by the colour bar) for the two minor-merger models 'gSadE001dir33' and 'gSadE006ret33', respectively, where $R_{\rm d}$ is the disc scale length, taken to be 3 kpc.

To quantify the strength of an $m = 1$ lopsidedness, we divide the disc into two regions: an inner part $0 \leq R/R_d \leq 5$ and an outer part $5 \leq R/R_d \leq 7$, where R_d is the disc scale length, chosen to be 3 kpc. This choice of inner and outer radial ranges is based on the TW analysis. The optimal slit length of ~ 14 pixels (see Section 4.4.2) mainly probes the inner disc. Dividing the disc in this way allows us to compare the lopsidedness within the region sampled by the TW method and in the outer parts beyond it.

For each simulation snapshot, we extracted the radial profile of the $m = 1$ Fourier amplitude, $A_1/A_0(R)$, and evaluated both the median and the integrated (trapezoidal) measures in the inner and outer disc regions. The median provides a measure of the typical asymmetry, while the integrated value captures the overall strength of the mode across each region. The integrated lopsidedness is computed using trapezoidal integration over radius, i.e.

$$\overline{\langle A_1/A_0 \rangle}_{\rm inn} = \frac{1}{R_{\rm max} - R_{\rm min}} \int_{R_{\rm min}}^{R_{\rm max}} \frac{A_1}{A_0}(R)\, dR, \tag{4.4}$$

and

$$\overline{\langle A_1/A_0 \rangle}_{\rm out} = \frac{1}{R_{\rm max} - R_{\rm min}} \int_{R_{\rm min}}^{R_{\rm max}} \frac{A_1}{A_0}(R)\, dR, \tag{4.5}$$

and the median lopsidedness is given by

$$\langle A_1/A_0 \rangle_{\rm inn} = \text{median}\big[A_1/A_0(R)\big]_{\rm inn}, \tag{4.6}$$

and

$$\langle A_1/A_0 \rangle_{\rm out} = \text{median}\big[A_1/A_0(R)\big]_{\rm out}, \tag{4.7}$$

respectively.

The relation between these two quantities is shown in Figure 4.4. The bottom panels, corresponding to the outer disc, show a strong correlation between

the median and integrated amplitudes, with Pearson correlation coefficients of $\rho = 0.987$ and $\rho = 0.97$ for the two models. This indicates that the lopsidedness in the outer region is well-behaved and consistently traced by both methods. Whereas the top panels, corresponding to the inner disc, show a larger scatter and a more distorted trend, with weaker correlations of $\rho = 0.666$ and $\rho = 0.425$. This is mainly due to the presence of a single spiral arm, which introduces additional asymmetry and affects the measurement in this region. Overall, the correlation is significantly stronger in the outer disc compared to the inner region.

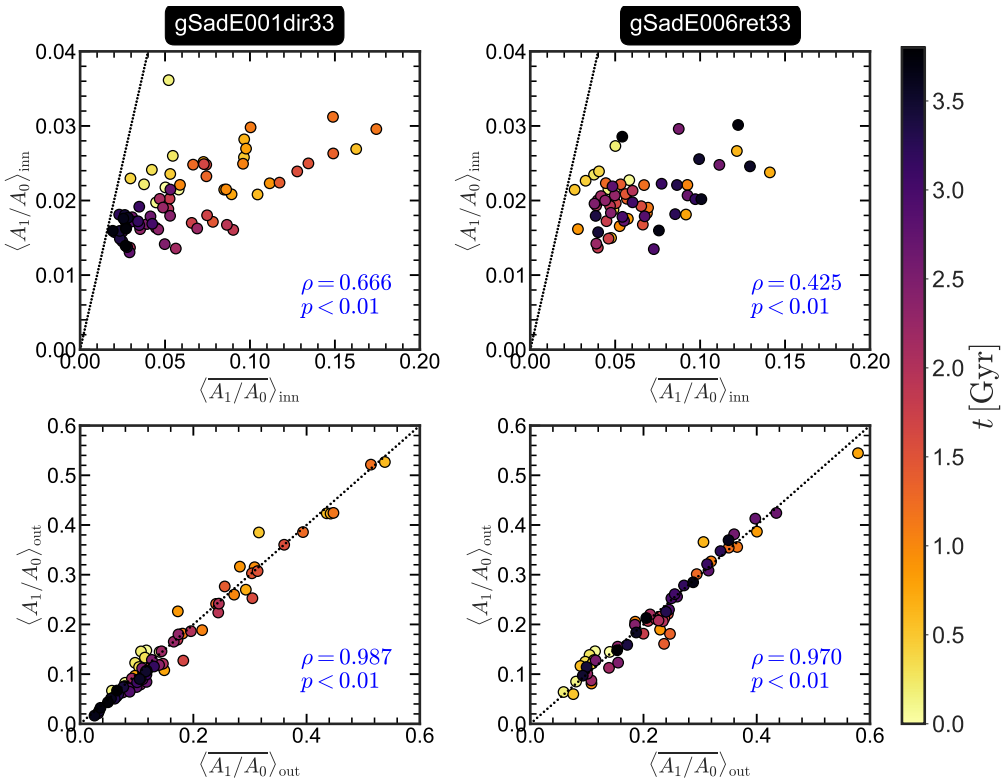


Figure 4.4: *Correlation between median and integrated an $m = 1$ amplitudes in inner and outer disc regions:* The top panels show the outer disc ($5 \leq R/R_d \leq 7$), while the bottom panels correspond to the inner disc ($0 \leq R/R_d \leq 5$), for the two models 'gSadE001dir33' (left) and 'gSadE006ret33' (right). Each point represents a different snapshot, with colour indicating the time evolution. The region shows a tighter correlation, while the inner region displays increased scatter due to the presence of a spiral arm. The Pearson correlation coefficient, ρ, is shown in each panel.

4.3 True bar pattern speed measurement - DSS method

In order to quantify the dynamical effect of the $m = 1$ lopsidedness on the bar pattern speed estimates from the TW method, first, we need to compute the 'true' bar pattern speed ($\Omega_{\rm bar,True}$). This, in turn, will provide the required benchmark to quantify biases (if any) in the bar pattern speed estimates from the TW method. In practice, often the bar pattern speed in simulations are estimated by tracking how the phase of the $m = 2$ Fourier mode evolves over time. In other words,

$$\Omega_{\rm bar} \approx \Omega_{\rm bar,FD} \equiv \frac{\Delta\phi_2}{\Delta t} \,. \tag{4.8}$$

Since the bar phase angle, ϕ_2 is periodic with a period of 2π, this method requires $\Omega_{\rm bar}\Delta t << \pi$ to unambiguously identify $\Delta\phi_2$. Since the models from the GalMer database we used in this work, do not have high output cadence (i.e. having long output intervals Δt), therefore, this method is not ideal to compute the values of $\Omega_{\rm bar,True}$ from the merger models considered here.

Instead, we use a more sophisticated Fourier-based method, called the DSS method (Dehnen, Semczuk, and Schönrich, 2022), which computes the bar pattern speed from a *single* snapshot. It has been demonstrated that this method is unbiased, precise, and consistent in the sense $\phi_2 = \int \Omega_{\rm bar}\, dt$. The detailed formulation is given in Dehnen, Semczuk, and Schönrich (2022). Here, for the sake of completeness, we briefly outline the method.

Let the disc be rotation is with respect to the z-axis, i.e. in azimuth φ and the density ρ is stationary in a rotating frame with angular speed $\Omega_{\rm bar}$. In other words, $\rho(R, z, \phi, t) = f(R, z, \phi - \psi)$ where $\psi(t) \equiv \int \Omega_{\rm bar}(t)\, dt$ denotes the instantaneous orientation of the rotation frame, and $\partial\rho/\partial t = -\Omega_{\rm bar}\, \partial\rho/\partial\varphi$. Combining this with the continuity equation, and after some algebraic manipulation we get

$$\Omega_{\rm bar} \int d^3\mathbf{x}\rho \frac{\partial w}{\partial \varphi} = \int d^3\mathbf{x}\rho \bar{\mathbf{v}}.\nabla w\,, \tag{4.9}$$

where w is a weight function. In a Fourier-based method, a natural choice for the weight function is $w(\mathbf{x}) = W(R)e^{-im\varphi}$ where m is the azimuthal wavenumber and $W \geq 0$ is some window function. Putting this in Eq. 4.9 we get

$$\Omega_{\rm bar} = \frac{\int d^3\mathbf{x}\rho \left[W\bar{\dot{\varphi}} + \frac{i}{m}\bar{v_R}(\partial W/\partial R)\right] e^{-im\varphi}}{\int d^3\mathbf{x}\rho W e^{-im\varphi}}\,. \tag{4.10}$$

If the density ρ remains stationary in the rotating frame, the R.H.S. of Eq.4.10 is real-valued. In the more general case,

$$\Omega_{\rm bar} + \frac{i}{m}\frac{\dot{\Sigma}_m}{\Sigma_m} = \frac{\int d^3\mathbf{x}\rho \left[W\bar{\dot{\varphi}} + \frac{i}{m}\bar{v_R}(\partial W/\partial R)\right] e^{-im\varphi}}{\int d^3\mathbf{x}\rho W e^{-im\varphi}}\,. \tag{4.11}$$

where Σ_m is the amplitude and ψ_m is the phase of $\hat{\Sigma}_m$, azimuthal Fourier transform of the window-averaged surface density $\Sigma(\varphi, t) \equiv \iint \rho W R dR dz$. For N-body models, the distribution function can be thought of as a sum of δ-peak, thereby resulting in the following substitutions $\int d^3\mathbf{x}\rho \to \sum_i \mu_i$ and $\int d^3\mathbf{x}\bar{v_R} \to \sum_i \mu_i \mathbf{v}_i$ where μ_i denotes the mass of the ith particle. Therefore, Eq. 4.11 reduces to

$$\Omega_{\rm bar} + \frac{i}{m}\frac{\dot{\Sigma}_m}{\Sigma_m} = \frac{\sum_i \mu_i \left[W_i\dot{\varphi}_i + \frac{i}{m}\dot{R}_i(\partial W/\partial R)_i\right] e^{-im\varphi_i}}{\sum_i \mu_i W_i e^{-im\varphi_i}}\,. \tag{4.12}$$

For real-valued $W(R)$, the corresponding Fourier amplitude, phase, and their time derivatives are

$$\begin{aligned} \Sigma_m &= \sqrt{C_m^2 + S_m^2}, & \frac{\dot{\Sigma}_m}{\Sigma_m} &= \frac{C_m\dot{C}_m + S_m\dot{S}_m}{C_m^2 + S_m^2} \\ \psi_m \frac{1}{m}\tan^{-1}\frac{S_m}{C_m}, & & \Omega_m &= \frac{C_m\dot{S}_m - S_m\dot{C}_m}{m(C_m^2 + S_m^2)} \end{aligned} \tag{4.13}$$

where

$$C_m \equiv \sum_i \mu_i W(\mathbf{x}_i) \cos m\varphi_i; \qquad S_m \equiv \sum_i \mu_i W(\mathbf{x}_i) \sin m\varphi_i \tag{4.14}$$

As each of the terms in Eq.4.14 is of the form $\sum_i p_i = N\langle p \rangle$, i.e. the sample mean, therefore, the variance can be estimated as

$$\sigma^2 \approx \frac{N}{N-1} \sum_i (p_i - \langle p \rangle)^2 \,. \tag{4.15}$$

Using these formulae, we calculated the true bar pattern speed, $\Omega_{\rm bar,True}$ for the $m = 2$ stellar bar, at different times (covering epochs before and after the merger) for both the minor merger models, namely, gSadE001dir33 and gSadE006ret33. This is shown is Figure 4.5. In the subsequent sections, we make use of these (true) bar pattern speed values as the 'benchmark' to quantify the plausible bias introduced by an $m = 1$ lopsidedness in bar pattern speed measurement via the TW method.

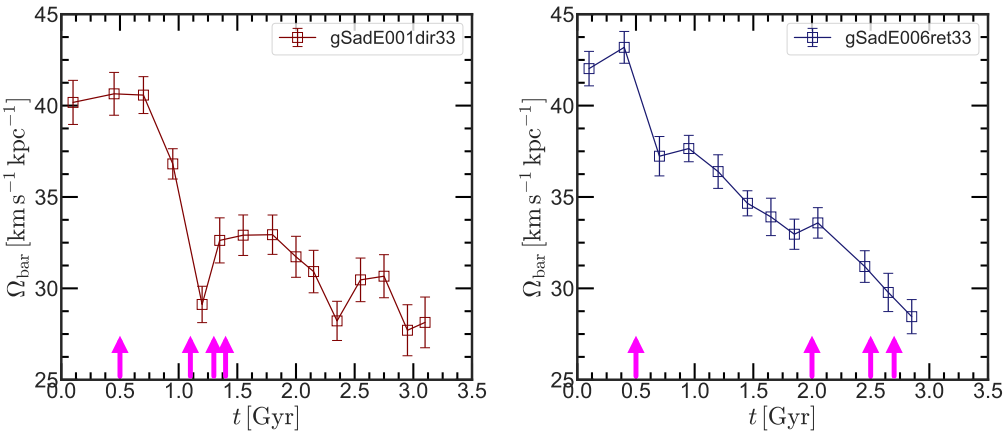


Figure 4.5: Temporal evolution of the pattern speed $\Omega_{\rm bar}$ (in km s^{-1} kpc^{-1}) over time (in Gyr) for two distinct minor merger models, 'gSadE001dir33' and 'gSadE006ret33'. Magenta arrows show the epochs of pericentre passage for both models.

4.4 Bar pattern speed via TW Method

After calculating the true bar pattern speed, $\Omega_{\rm bar,True}$, using the DSS method, we now turn to estimate the bar pattern speed using the Tremaine-Weinberg (TW) method. The primary goal of this section is to examine how the presence of an $m = 1$ lopsidedness affects the TW-based measurements, by directly comparing them with the true values derived earlier.

We begin by constructing the line-of-sight (LOS) maps from the intrinsic particle distribution (Section 4.4.1), as required for the application of the TW method. Using these, we first perform a sanity check to determine the optimal set of parameters, such as the slit length ($L_{\rm half}$) and the inclination (i).

Then, with this set-up in place, we begin with a symmetric disc in Section 4.4.2 as a reference, and gradually introduce an $m = 1$ lopsided asymmetry, moving from weak to intermediate and finally strong cases from Sections 4.4.3 - 4.4.5.

4.4.1 *Creating the LOS maps from intrinsic particle distribution*

In order to compare the simulated galaxy with observations, the intrinsic three-dimensional particle distribution is projected onto the plane of the sky to construct line-of-sight (LOS) maps. Each particle in the simulation is characterised by its position (x, y, z) and velocity (v_x, v_y, v_z) in the intrinsic coordinate system of the galaxy, where the x–y plane corresponds to the disc plane and the z axis is perpendicular to the disc.

To reproduce the orientation of an observed galaxy, the particle distribution is rotated using a set of rotation matrices. The inclination angle i determines the tilt of the galaxy relative to the observer's line of sight. This transformation can be written as

$$\mathbf{x}' = R_2 R_1 \mathbf{x}, \tag{4.16}$$

where $\mathbf{x} = (x, y, z)$ 'represents the intrinsic coordinates and $\mathbf{x}' = (x', y', z')$ 'represents the coordinates in the observer's frame. The matrix R_1 corresponds to a rotation that introduces the inclination i,

$$R_1 = \begin{bmatrix} 1 & 0 & 0 \\ 0 & \cos i & -\sin i \\ 0 & \sin i & \cos i \end{bmatrix}. \tag{4.17}$$

and,

$$R_2 = \begin{bmatrix} \sin\theta & 0 & \cos\theta \\ 0 & 1 & 0 \\ -\cos\theta & 0 & \cos\theta \end{bmatrix}. \tag{4.18}$$

After the rotation, the x' and y' axes define the plane of the sky, while the z' axis corresponds to the line of sight. The projected surface density map is obtained by integrating the particle density along the line of sight.

$$\Sigma(x', y') = \int \rho(x', y', z')\, dz', \tag{4.19}$$

which in practice is computed by summing the masses of all particles that fall within each pixel of the projected grid. Similarly, the line-of-sight velocity map is constructed by computing the velocity component along the LOS direction. The LOS velocity of each particle is given by

$$v_{\mathrm{LOS}} = \vec{v} \cdot \hat{n}_{\mathrm{LOS}}, \tag{4.20}$$

Where $\vec{v}$ is the particle velocity vector and $\hat{n}_{\mathrm{LOS}}$ is the unit vector along the line of sight. The mean velocity in each pixel is then obtained using a density-weighted average.

$$V_{\mathrm{LOS}}(x', y') = \frac{\int \rho v_{\mathrm{LOS}} dz'}{\int \rho dz'}. \tag{4.21}$$

By repeating this procedure for different inclination angles, we produced a series of projected maps, as shown in Figure 4.6, that show how the galaxy would appear to an observer at different viewing angles.

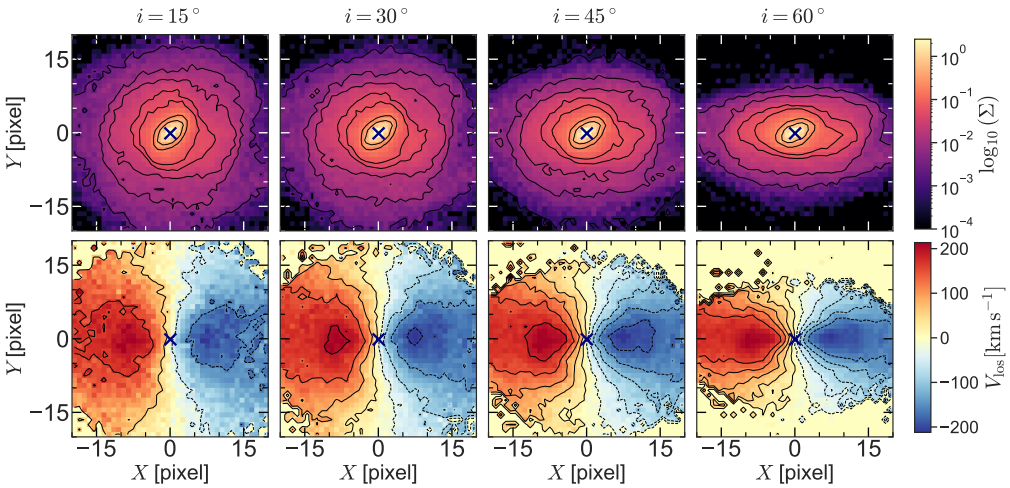


Figure 4.6: Line-of-sight (LOS) maps constructed from the intrinsic particle distribution. The top panels show the projected surface density maps, while the bottom panels show the corresponding LOS velocity maps. The columns represent inclination angles of 15°, 30°, 45°, and 60° respectively. The cross symbol '×'(in blue) marks the photometric centre of the galaxy. Black contours denote constant levels, and the colour bars indicate the plotted quantity. Shown for the model 'gSaadE001dir33'

4.4.2 The case with no lopsidedness – sanity check

Before applying the TW method to minor merger models, we first test it in a case where the galaxy has no lopsidedness. For this, we select a snapshot prior to the first pericentric passage, when the disc is close to axisymmetric. First, we begin by determining optimal parameters for TW measurement, such as ($L_{\rm half}$), inclination (i). The results are shown in Fig. 4.7. To construct these plots, we apply the TW method multiple times by varying one parameter at a time while keeping the others fixed. In the left panel, we change the slit half-length ($L_{\rm half}$) and compute the corresponding bar pattern speed for each choice. The measurements become stable beyond a slit half-length of $\sim$ 14 pixels, which we adopt as the optimal choice. In the right panel, we vary the disc inclination and again compute the pattern speed. The results remain stable around an inclination of $\sim$ 15°, which is taken as the preferred inclination.

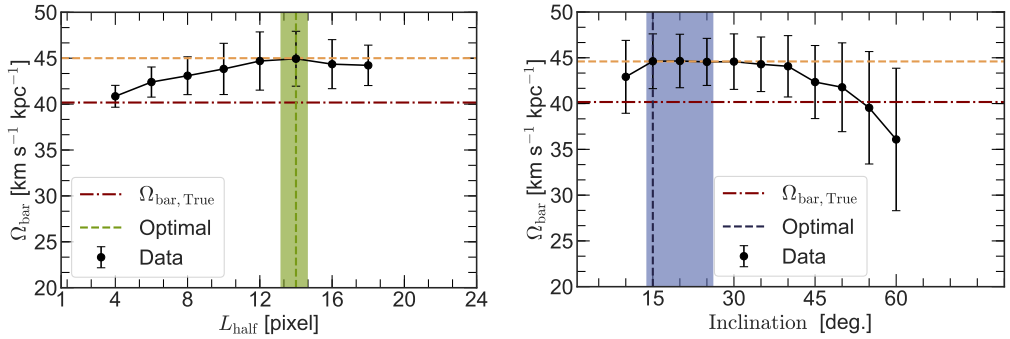


Figure 4.7: *Left panel* shows $\Omega_{\rm bar,TW}$ as a function of slit half-length ($L_{\rm half}$, stabilising beyond $\sim$ 14 pixels, taken as the optimal length. *Right panel* shows $\Omega_{\rm bar,TW}$ as a function of disc inclination, stabilising over a range around 15°. Shaded regions denote the stable ranges.

Using these optimal parameters, we apply the TW method to the axisymmet-

ric case. Parallel slits of length ∼ 14 pixels are placed across the disc, aligned with the galaxy's major axis (taken to be along the x-axis at 0° in the LOS maps). The slits are positioned symmetrically above and below the kinematic centre, with the central slit passing through it. The luminosity-weighted mean position, $\langle X \rangle$, and velocity, $\langle V_{\rm LOS} \rangle$, are then computed for each slit. The relation between these quantities, shown in Figure 4.8, is fitted with a straight line, whose slope gives the bar pattern speed.

Following this procedure, we obtain $\Omega_{\rm bar,TW} \approx 39.85 \pm 1.98$ km s^{-1} kpc^{-1}, which is in close agreement with the true value, $\Omega_{\rm bar,True} \approx 40.2 \pm 1.2$ km s^{-1} kpc^{-1}, with a difference of ~ 0.5 km s^{-1} kpc^{-1}. Since the disc is axisymmetric, the TW method closely reproduces the true value. This gives us confidence in the reference values, which will be used for comparison in the following cases.

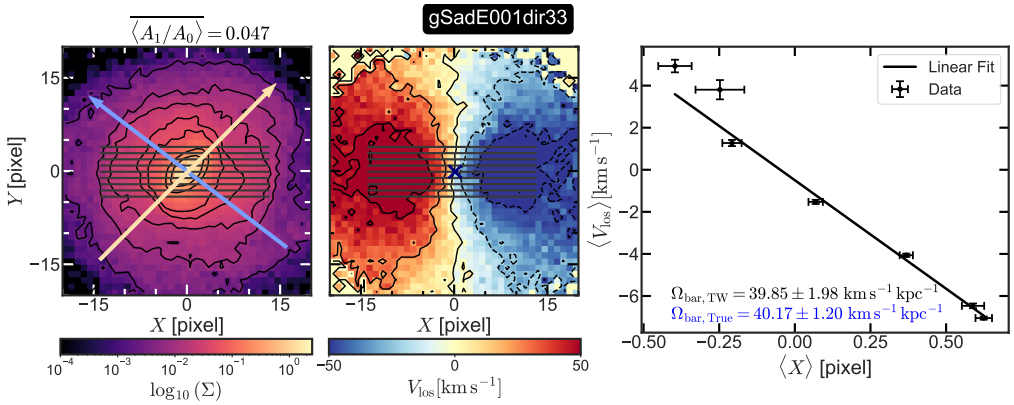


Figure 4.8: *Case with no lopsidedness: Left* and *middle* panels show the line-of-sight ($i = 15°$) density and velocity maps, respectively. Black solid lines denote the contours of constant density (*left panel*) and $V_{\rm LOS}$ (*middle panel*), respectively. Horizontal black lines denote the slit positions and '×' denotes the photometric centre. *Right panel:* luminosity-weighted position $\langle X \rangle$ and the y-axis represents the luminosity-weighted velocity $\langle V \rangle$ as well as the best-fit slope to derive the bar pattern speed ($\Omega_{\rm bar,TW}$) via the TW method. In the absence of lopsidedness, the TW method recovers the true bar pattern speed ($\Omega_{\rm bar,true}$) within 2 km s^{-1} kpc^{-1}.

4.4.3 *The Case with Weak lopsidedness*

We begin with a case in which the inner disc shows only weak non-axisymmetry. The top-left panels of Figure 4.9 illustrate the line-of-sight density and velocity maps, where yellow arrows indicate the orientation of the bar and blue arrows mark the direction of the lopsidedness. For *gSadE001dir33*, we select a snapshot at $t = 0.45$ Gyr. At this stage, the inner asymmetry is weak, with $\overline{\langle A_1/A_0 \rangle}_{\rm inn} = 0.057$. Using the TW method, we calculate $\Omega_{\rm bar,TW} \approx 33.3 \pm 1.87$ km s^{-1} kpc^{-1}, while the true value is $\Omega_{\rm bar,True} \approx 40.64 \pm 1.17$ km s^{-1} kpc^{-1}. A similar behaviour is seen in the *gSadE006ret33* model. Here, we consider a snapshot at $t = 1.2$ Gyr, where the inner asymmetry remains weak with value $\overline{\langle A_1/A_0 \rangle}_{\rm inn} = 0.0657$. The TW method yields $\Omega_{\rm bar,TW} \approx 29$ km s^{-1} kpc^{-1}, compared to the true value $\Omega_{\rm bar,True} \approx 36.38 \pm 1.63$ km s^{-1} kpc^{-1}, resulting in a deviation of about 18 – 20%.

This behaviour is not restricted to these snapshots. Other snapshots in *gSadE001dir33* at $t = 2.55$, and 3.1 Gyr, and in *gSadE006ret33* at $t = 0.4$, 1.45, and 1.65 Gyr, also shows a similar strength of inner lopsidedness. In each case, the TW method gives pattern speeds that differ from the true values by about

20%. Despite these differences, the overall behaviour indicates that, within this level of an $m = 1$ asymmetry, the TW method is still able to recover the bar pattern speed reasonably well, with only modest deviations from the true values. Following this, we move to the next case where the disc shows an intermediate level of an $m = 1$ lopsidedness.

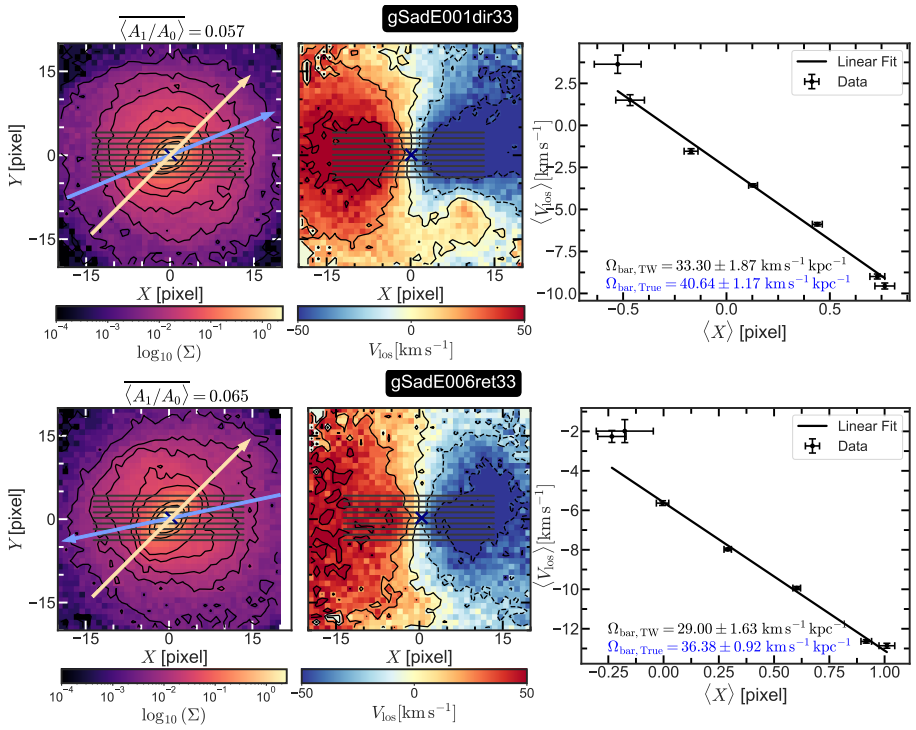


Figure 4.9: *Case with weak lopsidedness: Left* and *middle* panels show the line-of-sight ($i = 15°$) density and velocity maps, respectively. Black solid lines denote the contours of constant density (*left panel*) and $V_{\rm LOS}$ (*middle panel*), respectively. Horizontal black lines denote the slit positions and '×' denotes the photometric centre. *Right panel:* luminosity-weighted position $\langle X \rangle$ and the y-axis represents the luminosity-weighted velocity $\langle V \rangle$ as well as the best-fit slope to derive the bar pattern speed ($\Omega_{\rm bar,TW}$) via the TW method. In weak lopsidedness, TW closely matches the true value with a small offset, a slight overestimation in 'gSadE006ret33' and underestimation in 'gSadE001dir33'.

4.4.4 The Case with Intermediate lopsidedness

We then examine a disc where it exhibits an intermediate level of an $m = 1$ lopsidedness. In this case, the TW method does not retain the same level of robustness seen earlier. The $\langle V_{\rm LOS} \rangle$–$\langle X \rangle$ relation shows increased scatter, and the data points deviate more noticeably from a clear linear trend, as seen in Figure 4.10.

Applying the TW method to the *gSadE001dir33* model at $t = 0.7$ Gyr, with $\overline{\langle A_1/A_0 \rangle}_{\rm inn} = 0.074$, we obtain $\Omega_{\rm bar,TW} \approx 49.51 \pm 1.24$ km s^{-1} kpc^{-1}, compared to the true value $\Omega_{\rm bar,True} \approx 40.57 \pm 1.01$ km s^{-1} kpc^{-1}, giving a deviation of $\Omega_{\rm bar,True} - \Omega_{\rm bar,TW} \approx -8.94$ km s^{-1} kpc^{-1}. A similar but stronger discrepancy is found in the *gSadE006ret33* model at $t = 2.45$ Gyr, with $\overline{\langle A_1/A_0 \rangle}_{\rm inn} = 0.079$, where $\Omega_{\rm bar,TW} \approx 49.13 \pm 8.2$ km s^{-1} kpc^{-1}, while the true value is $\Omega_{\rm bar,True} \approx 31.19 \pm 0.86$ km s^{-1} kpc^{-1}, resulting in $\Omega_{\rm bar,True} - \Omega_{\rm bar,TW} \approx$

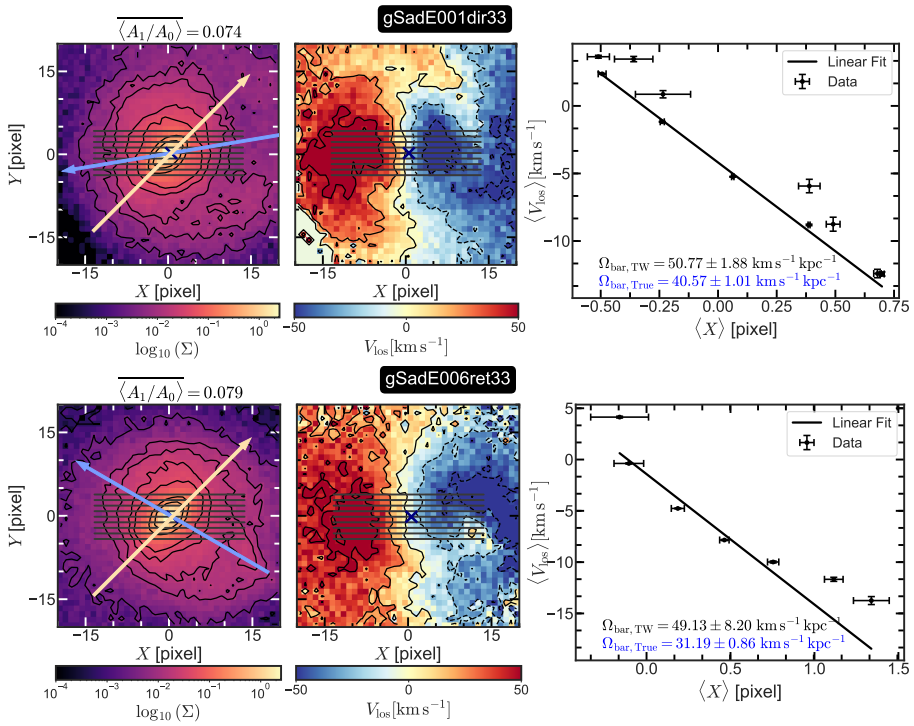


Figure 4.10: *Case with intermediate lopsidedness: Left* and *middle* panels show the line-of-sight (i = 15°) density and velocity maps, respectively. Black solid lines denote the contours of constant density (*left panel*) and $V_{\rm LOS}$ (*middle panel*). Horizontal black lines denote the slit positions and '×' denotes the photometric centre. *Right panel:* luminosity-weighted position $\langle X \rangle$ and luminosity-weighted velocity $\langle V \rangle$ with the best-fit slope giving $\Omega_{\rm bar,TW}$. In intermediate lopsidedness, where slit orientations are not directly aligned with the lopsided component, the TW method still shows noticeable deviation from the true value.

$-17.94\,\mathrm{km\,s^{-1}\,kpc^{-1}}$.

Although the lopsidedness is not aligned with the slit orientation, its effect is clearly reflected in the TW relation, leading to systematic offsets in the derived values. A similar trend is also observed at $t = 0.95$ and 2.15 Gyr for *gSadE001dir33*, and at $t = 1.85$ Gyr for *gSadE006ret33*. Overall, the TW estimates exceed the true pattern speeds by ~ 9 to $18\,\mathrm{km\,s^{-1}\,kpc^{-1}}$, demonstrating that even moderate lopsidedness can significantly bias the measurement. This naturally leads us to more extreme configurations, which we explore in the next section. We examine the case where the disc exhibits a strong an $m = 1$ lopsidedness.

4.4.5 *The case with Strong lopsidedness*

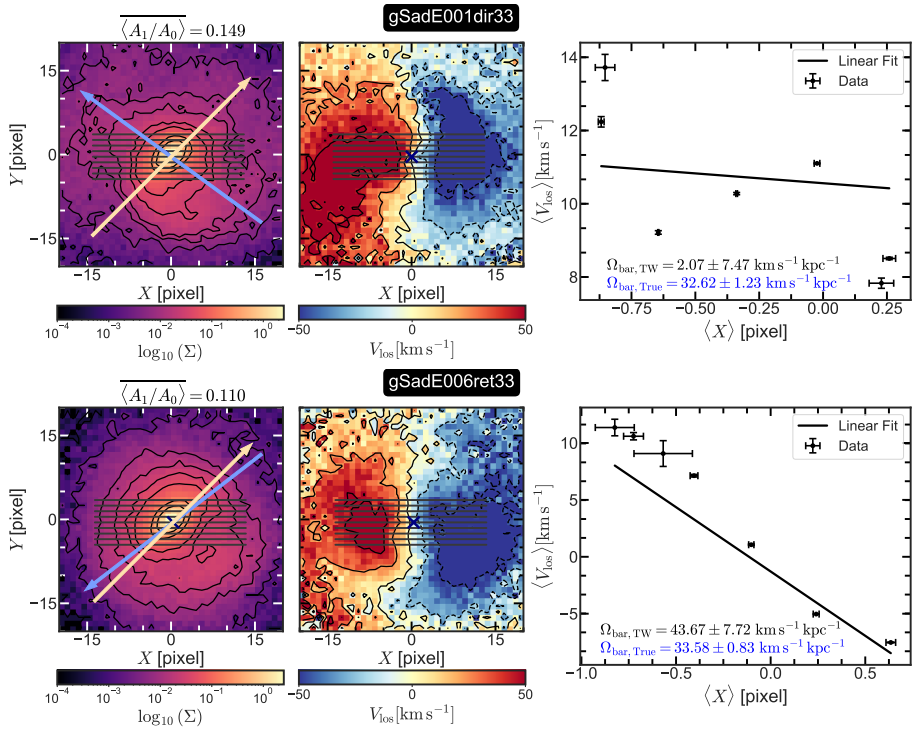


Figure 4.11: *Case with strong lopsidedness: Left* and *middle* panels show the line-of-sight ($i = 15°$) density and velocity maps, respectively. Black solid lines denote the contours of constant density (*left panel*) and $V_{\rm LOS}$ (*middle panel*). Horizontal black lines denote the slit positions and '×' denotes the photometric centre. *Right panel:* luminosity-weighted position $\langle X\rangle$ and luminosity-weighted velocity $\langle V\rangle$ with the best-fit slope giving $\Omega_{\rm bar,TW}$. In strong lopsidedness, TW deviates significantly from the true value, showing large overestimation in 'gSadE006ret33' and underestimation in 'gSadE001dir33'.

We finally consider snapshots where the disc shows a strong $m = 1$ lopsidedness. In this regime, the effect of asymmetry becomes dominant, and the TW method no longer shows a well-defined linear behaviour. The $\langle V_{\rm LOS}\rangle$–$\langle X\rangle$ relation displays a large scatter, as seen in Figure 4.11, indicating a significant deviation from the expected behaviour.

For the *gSadE001dir33* model at $t = 1.35$ Gyr, with $\overline{\langle A_1/A_0\rangle}_{\rm inn} = 0.149$, the TW method gives $\Omega_{\rm bar,TW} \approx 2.07 \pm 7.47\,\mathrm{km\,s^{-1}\,kpc^{-1}}$, while the true value is $\Omega_{\rm bar,True} \approx 32.62 \pm 1.23\,\mathrm{km\,s^{-1}\,kpc^{-1}}$, resulting in an underestimation of $\sim 93\%$.

In contrast, for the *gSadE006ret33* model at $t = 0.7$ Gyr, with $\overline{\langle A_1/A_0 \rangle}_{\rm inn} = 0.11$, the TW method yields $\Omega_{\rm bar,TW} \approx 43.67 \pm 7.72\ {\rm km\,s^{-1}\,kpc^{-1}}$, compared to the true value $\Omega_{\rm bar,True} \approx 33.58 \pm 0.83\ {\rm km\,s^{-1}\,kpc^{-1}}$, leading to an overestimation of $\sim 30\%$.

This trend is also seen in other snapshots. In the *gSadE001dir33* model, at $t = 1.2$, and 1.55 Gyr, and in the *gSadE006ret33* model at $t = 0.95$ Gyr, also exhibit strong lopsidedness. In all these cases, the TW method exhibits large scatter and strong departures from the true pattern speed, yielding both underestimates and overestimates. This demonstrates that strong lopsidedness fundamentally breaks the assumptions of the TW method, marking a regime where it cannot reliably recover the bar pattern speed.

Across the different regimes explored above, from weak to strong an $m = 1$ lopsidedness, the TW method shows a clear decline in accuracy, performing well only in near-axisymmetric discs. Significant deviations appear in intermediate and strong cases. To better understand this behaviour, we now examine how the TW-derived and True bar pattern speeds evolve over time during the merger, as shown in Figure 4.12, which compares $\Omega_{\rm bar,TW}$ and $\Omega_{\rm bar,True}$ with colour indicating time, along with Figure 4.2, which shows the orbital separation. At early times, the disc is nearly axisymmetric and the TW estimates agree with the true values. As the satellite undergoes pericentric passages, strong non-axisymmetric perturbations develop, increasing an $m = 1$ lopsidedness and leading to scatter and deviations from the one-to-one relation. For *gSadE001dir33*, the merger remnant relaxes and the TW and true values realign. Whereas, for *gSadE006ret33*, the delayed merger maintains asymmetry, and the TW estimates remain offset at later times.

Overall, this comparison demonstrates that the reliability of the TW method is closely linked to the dynamical state of the system, it performs well in nearly symmetric phases but progressively fails during and after strong interactions associated with pericentric passages.

This study demonstrates that the presence of an $m = 1$ lopsidedness introduces a systematic bias in TW measurement. While the TW method performs well for a symmetric disc, its accuracy decreases with increasing asymmetry, leading to large and inconsistent deviations. By comparing DSS-based true values, we find that the disc asymmetry plays a key role in driving these differences. This highlights a limitation of the TW method in an idealised system and helps in interpreting such measurements more reliably.

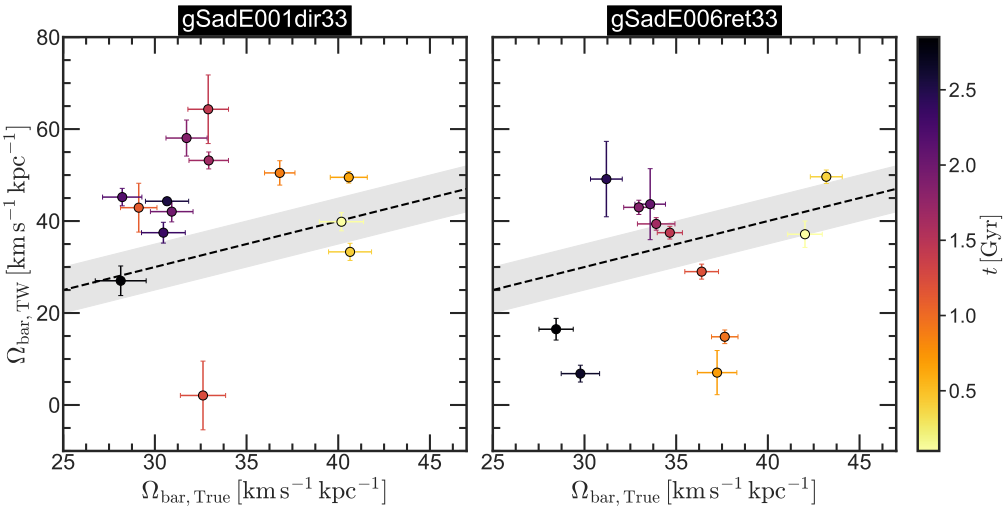


Figure 4.12: *Comparison of TW-derived and true bar pattern speeds:* Left and right panels show the relation between the TW-derived bar pattern speed, $\Omega_{\rm bar,TW}$, and the true value, $\Omega_{\rm bar,True}$, for the 'gSadE001dir33' and 'gSadE006ret33' models, respectively. Each point corresponds to a different snapshot, with colour indicating the time evolution of the system. The dashed line denotes the one-to-one relation, while the shaded region highlights the expected range of agreement.

Chapter 5

Summary and Future scope

In this thesis, we have investigated how the presence of an $m = 1$ lopsidedness affects the measurement of bar pattern speed in disc galaxies. The study was motivated by the fact that, although the Tremaine–Weinberg (TW) method is widely used and model-independent, it relies on the assumption that the underlying disc is axisymmetric. However, both observations and simulations show that many galaxies exhibit significant lopsidedness, along with the bar.

To address this, we analysed two minor merger models from the GalMer database, where such asymmetries naturally develop over time. The true bar pattern speed, $\Omega_{\rm bar,True}$, was measured using the DSS method from the temporal evolution of the $m = 2$ Fourier phase. This provided a reliable reference against which the TW-derived values could be directly compared. We first established that for an pure axisymmetric disc, the bar pattern speed value obtained from the TW mehtod agrees fairly well with in the true bat pattern speed value. This conferm the validity of the method when its assumptions are satisfied. We then systematically explored cases with increasing strength of an $m = 1$ lopsidedness.

In the weak lopsidedness regime ($\langle A_1/A_0 \rangle \lesssim 0.1$), the TW method continues to recover values close to $\Omega_{\rm bar,True}$, with only small deviations. As the strength of lopsidedness increases to intermediate levels, the TW relation begins to show noticeable scatter, and the derived values deviate by $\sim$ 20%–30% in some cases. In the strong lopsidedness regime, the deviations become significant, with differences reaching up to $\sim$ 50%–98%, and the TW relation no longer follows a clear linear trend. This indicates that the $m = 1$ lopsidedness disc asymmetry plays a dominant role in driving the bias in the TW measurement.

Overall, our results demonstrate that the TW method remains reliable only when the disc is close to axisymmetry. As the level of lopsidedness increases, the method becomes increasingly sensitive to asymmetries, leading to large scatter and inconsistent values. Since such asymmetries are common in galaxies undergoing interactions or minor mergers, this highlights an important limitation of the TW method in idealised conditions.

This analysis can be extended to cosmological simulations, such as the IllustrisTNG simulations, which model galaxy formation and evolution and provide large catalogues of galaxies. From these, lopsided systems will be identified and analysed using the same methodology. This will allow us to test the TW measurement in a more realistic population where non-axisymmetric structures arise naturally. A further step is to study a larger sample of such galaxies across different masses and merger histories. This will enable us to quantify how the strength of an $m = 1$ lopsidedness correlates with deviations in TW-derived pattern speeds and to assess the reliability of the method in non-axisymmetric systems.

REFERENCES

Aguerri, J. A. L. (Nov. 1999a). "A strong correlation between bar strength and global star forming activity in isolated barred galaxies". In: *Astronomy & Astrophysics* 351, pp. 43–46.

— (1999b). "A strong correlation between bar strength and global star forming activity in isolated barred galaxies". In: *Astronomy & Astrophysics* 351, pp. 43–46.

Aguerri, J. A. L. et al. (2015). "Bar pattern speeds in CALIFA galaxies". In: *Astronomy & Astrophysics* 576, A102. DOI: 10.1051/0004-6361/201425221.

Aguerri, J. A. L., J. E. Beckman, and M. Prieto (1998). "The phase shift of spiral arms across corotation in galaxies". In: *The Astronomical Journal* 116.5, pp. 2136–2149. DOI: 10.1086/300567.

Aguerri, J. A. L., Victor P. Debattista, and Enrico Maria Corsini (2003). "Measurement of fast bars in a sample of early-type barred galaxies". In: *Monthly Notices of the Royal Astronomical Society* 338.2, pp. 465–480. DOI: 10.1046/j.1365-8711.2003.06067.x. URL: https://doi.org/10.1046/j.1365-8711.2003.06067.x.

Aguerri, J. A. L., J. Méndez-Abreu, and E. M. Corsini (Jan. 2009). "The population of barred galaxies in the local universe: I. Detection and characterisation of bars". In: *Astronomy & Astrophysics* 495.2, pp. 491–504. DOI: 10.1051/0004-6361:200810931.

Aguerri, J. A. L., C. Muñoz-Tuñón, et al. (Sept. 2000). "Characterizing bar structures: application to NGC 1300, NGC 7479 and NGC 7723". In: *Astronomy & Astrophysics* 361, pp. 841–849.

Angiras, R. A. et al. (2006). "Origin of disc lopsidedness in the Eridanus group of galaxies". In: *Monthly Notices of the Royal Astronomical Society* 369.4, pp. 1849–1857. DOI: 10.1111/j.1365-2966.2006.10418.x. URL: https://doi.org/10.1111/j.1365-2966.2006.10418.x.

Athanassoula, E. (1992). "The existence and shapes of dust lanes in galactic bars". In: *Monthly Notices of the Royal Astronomical Society* 259, pp. 328–352.

— (Dec. 2002). "Formation and Evolution of Bars in Disc Galaxies". In: *Disks of Galaxies: Kinematics, Dynamics and Peturbations*. Ed. by E. Athanassoula, A. Bosma, and R. Mujica. Vol. 275. Astronomical Society of the Pacific Conference Series, pp. 141–152. DOI: 10.48550/arXiv.astro-ph/0209438. arXiv: astro-ph/0209438 [astro-ph].

— (June 2003). "What determines the strength and the slowdown rate of bars?" In: *Monthly Notices of the Royal Astronomical Society* 341.4, pp. 1179–1198. DOI: 10.1046/j.1365-8711.2003.06473.x. arXiv: astro-ph/0302519 [astro-ph].

Athanassoula, E. and A. Misiriotis (2002). "Morphology, photometry and kinematics of N-body bars: the effects of disc thickness and velocity anisotropy". In: *Monthly Notices of the Royal Astronomical Society* 330, pp. 35–52.

Baldwin, J. E., D. Lynden-Bell, and R. Sancisi (Nov. 1980). "Lopsided galaxies". In: *Monthly Notices of the Royal Astronomical Society* 193.2, pp. 313–319.

ISSN: 0035-8711. DOI: 10.1093/mnras/193.2.313. URL: https://doi.org/10.1093/mnras/193.2.313.

Barazza, Fabio D., Shardha Jogee, and Irina Marinova (Mar. 2008). "Bars in Disk-dominated and Bulge-dominated Galaxies at z 0: New Insights from 3600 SDSS Galaxies". In: *The Astrophysical Journal* 675.2, p. 1194. DOI: 10.1086/526510.

Barnes, Josh and Piet Hut (Dec. 1986). "A hierarchical O(N log N) force-calculation algorithm". In: *Nature* 324.6096, pp. 446–449. DOI: 10.1038/324446a0.

Barway, Sudhanshu, Yogesh Wadadekar, and Ajit K. Kembhavi (Jan. 2011). "Bar fraction in lenticular galaxies: dependence on luminosity and environment". In: *Monthly Notices of the Royal Astronomical Society* 410.1, pp. L18–L22. DOI: 10.1111/j.1745-3933.2010.00970.x. arXiv: 1010.2906 [astro-ph.CO].

Binney, J. and S. Tremaine (2008). *Galactic Dynamics*. 2nd ed. Princeton University Press.

Binney, James et al. (Sept. 1991). "Understanding the kinematics of Galactic Centre gas". In: *Monthly Notices of the Royal Astronomical Society* 252.2, pp. 210–218. ISSN: 0035-8711. DOI: 10.1093/mnras/252.2.210. eprint: https://academic.oup.com/mnras/article-pdf/252/2/210/3932122/mnras252-0210.pdf. URL: https://doi.org/10.1093/mnras/252.2.210.

Borodina, Olga, Thomas G Williams, et al. (July 2023a). "On the Tremaine–Weinberg method: how much can we trust gas tracers to measure pattern speeds?" In: *Monthly Notices of the Royal Astronomical Society* 524.3, pp. 3437–3445. ISSN: 1365-2966. DOI: 10.1093/mnras/stad2068. URL: http://dx.doi.org/10.1093/mnras/stad2068.

— (Sept. 2023b). "On the Tremaine-Weinberg method: how much can we trust gas tracers to measure pattern speeds?" In: *Monthly Notices of the Royal Astronomical Society* 524.3, pp. 3437–3445. DOI: 10.1093/mnras/stad2068. arXiv: 2306.17780 [astro-ph.GA].

Bosma, A. (Dec. 1981). "21-cm line studies of spiral galaxies. I. Observations of the galaxies NGC 5033, 3198, 5055, 2841, and 7331." In: *The Astrophysical Journal* 86, pp. 1791–1824. DOI: 10.1086/113062.

Bournaud, F. et al. (Aug. 2005). "Lopsided spiral galaxies: evidence for gas accretion". In: *Astronomy & Astrophysics* 438.2, pp. 507–520. DOI: 10.1051/0004-6361:20052631. eprint: astro-ph/0503314. URL: https://ui.adsabs.harvard.edu/abs/2005A&A...438..507B.

Braun, R. (Dec. 1995). "Resolved atomic super-clouds in spiral galaxies." In: *Astronomy & Astrophysics Supplement Series* 114, p. 409. DOI: 10.48550/arXiv.astro-ph/9512085. arXiv: astro-ph/9512085 [astro-ph].

Bundy, K. et al. (2015). "Overview of the SDSS-IV MaNGA Survey: Mapping Nearby Galaxies at Apache Point Observatory". In: *The Astrophysical Journal* 798.1, p. 7. DOI: 10.1088/0004-637X/798/1/7.

Buta, R. (1986). "The structure and dynamics of resonance rings in barred galaxies". In: *The Astrophysical Journal Supplement Series* 61, pp. 609–665. DOI: 10.1086/191122.

Buta, R. J. and X. Zhang (2009). "The potential-density phase-shift method for determining bar and spiral pattern speeds". In: *The Astrophysical Journal Supplement Series* 182.2, pp. 559–583. DOI: 10.1088/0067-0049/182/2/559.

Canzian, B. (1993). "Pattern speeds of spiral structure in galaxies". In: *The Astrophysical Journal* 414, pp. 487–496. DOI: 10.1086/173099.

Casertano, S. and P. Hut (Nov. 1985). "Core radius and density measurements in N-body experiments Connections with theoretical and observational definitions". In: *The Astrophysical journal* 298, pp. 80–94. DOI: 10.1086/163589.

Chemin, L. and O. Hernandez (2009). "A slow bar in a dark matter dominated galaxy". In: *Astronomy & Astrophysics* 499, pp. L25–L28. DOI: 10.1051/0004-6361/200912019.

Chilingarian, I. V. et al. (Sept. 2010). "The GalMer database: Galaxy Mergers in the Virtual Observatory". In: *Astronomy & Astrophysics* 518, A61, A61. DOI: 10.1051/0004-6361/201014459. arXiv: 1003.3243 [astro-ph.CO].

Collaboration, Euclid et al. (2026). *Euclid preparation. Impact of galaxy intrinsic alignment modelling choices on Euclid 3x2pt cosmology*. arXiv: 2602.16448 [astro-ph.CO]. URL: https://arxiv.org/abs/2602.16448.

Combes, F., C. Dupraz, and M. Gerin (1990). *Gas Dynamics in a Tidal Interaction: Formation of Rings*. Ed. by Roland Wielen. Berlin, Heidelberg.

Combes, F. and R. H. Sanders (Mar. 1981). "Formation and properties of persisting stellar bars." In: *Astronomy & Astrophysics* 96, pp. 164–173.

Contopoulos, G. (Jan. 1980). "How far do bars extend". In: *Astronomy & Astrophysics* 81.1-2, pp. 198–209.

Corsini, E. M., J. A. L. Aguerri, and V. P. Debattista (Jan. 2003). "Fast bars in early-type barred galaxies". In: *Memorie della Società Astronomica Italiana* 74, p. 464.

Corsini, E. M., J. A. L. Aguerri, Victor P. Debattista, et al. (2007). "The Bar Pattern Speed of Dwarf Galaxy NGC 4431". In: *The Astrophysical Journal* 659.2, pp. L121–L124. DOI: 10.1086/518035.

Corsini, Enrico M. (2011). "Measuring the Pattern Speed of Bars". In: *Memorie della Società Astronomica Italiana Supplement* 18, pp. 23–37. URL: https://ui.adsabs.harvard.edu/abs/2011msais..18...23C.

Costantin, Luca et al. (Nov. 2023). "A Milky Way-like barred spiral galaxy at a redshift of 3". In: *Nature* 623.7987, pp. 499–501. ISSN: 1476-4687. DOI: 10.1038/s41586-023-06636-x. URL: http://dx.doi.org/10.1038/s41586-023-06636-x.

Croom, Scott M. et al. (Mar. 2012). "The Sydney-AAO Multi-object Integral field spectrograph". In: *Monthly Notices of the Royal Astronomical Society* 421.1, pp. 872–893. DOI: 10.1111/j.1365-2966.2011.20365.x. arXiv: 1112.3367 [astro-ph.CO].

Cuomo, Virginia et al. (2021). "Bar pattern speeds in CALIFA galaxies - III. Solving the puzzle of ultrafast bars". In: *Astronomy & Astrophysics* 649, A30. DOI: 10.1051/0004-6361/202040261. URL: https://doi.org/10.1051/0004-6361/202040261.

Debattista, Victor P. (July 2003). "On position angle errors in the Tremaine-Weinberg method". In: *Monthly Notices of the Royal Astronomical Society*

342.4, pp. 1194–1204. DOI: 10.1046/j.1365-8711.2003.06620.x. arXiv: astro-ph/0401137 [astro-ph].

Debattista, Victor P., Enrico Maria Corsini, and J. A. L. Aguerri (2002). "A fast bar in the post-interaction galaxy NGC 1023". In: *Monthly Notices of the Royal Astronomical Society* 332.1, pp. 65–77. DOI: 10.1046/j.1365-8711.2002.05269.x. URL: https://doi.org/10.1046/j.1365-8711.2002.05269.x.

Debattista, Victor P., Lucio Mayer, et al. (July 2006). "The Secular Evolution of Disk Structural Parameters". In: *The Astrophysical Journal* 645.1, pp. 209–227. DOI: 10.1086/504147. arXiv: astro-ph/0509310 [astro-ph].

Debattista, Victor P. and J. A. Sellwood (Nov. 2000). "Constraints from Dynamical Friction on the Dark Matter Content of Barred Galaxies". In: *The Astrophysical Journal* 543.2, pp. 704–721. DOI: 10.1086/317148. arXiv: astro-ph/0006275 [astro-ph].

Debattista, Victor P. and T. B. Williams (2004). "Fabry-Perot Absorption-Line Spectroscopy of NGC 7079: Kinematics and Bar Pattern Speed". In: *The Astrophysical Journal* 605.2, pp. 714–724. DOI: 10.1086/382585.

Dehnen, Walter (Feb. 2000). "The Effect of the Outer Lindblad Resonance of the Galactic Bar on the Local Stellar Velocity Distribution". In: *The Astrophysical Journal* 119.2, pp. 800–812. DOI: 10.1086/301226. arXiv: astro-ph/9911161 [astro-ph].

Dehnen, Walter, Marcin Semczuk, and Ralph Schönrich (Nov. 2022). "Measuring bar pattern speeds from single simulation snapshots". In: *Monthly Notices of the Royal Astronomical Society* 518.2, pp. 2712–2718. ISSN: 1365-2966. DOI: 10.1093/mnras/stac3184. URL: http://dx.doi.org/10.1093/mnras/stac3184.

Di Matteo, P. et al. (June 2007). "Star formation efficiency in galaxy interactions and mergers: a statistical study". In: *Astronomy & Astrophysics* 468, pp. 61–81. DOI: 10.1051/0004-6361:20066676. arXiv: astro-ph/0703126 [astro-ph].

Donohoe-Keyes, C E et al. (Sept. 2019). "Redistribution of stars and gas in the star formation deserts of barred galaxies". In: *Monthly Notices of the Royal Astronomical Society* 489.4, pp. 4992–5003. ISSN: 1365-2966. DOI: 10.1093/mnras/stz2474. URL: http://dx.doi.org/10.1093/mnras/stz2474.

Efstathiou, G., G. Lake, and J. Negroponte (June 1982). "The stability and masses of disc galaxies." In: *Monthly Notice of the Royal Astronomical society* 199, pp. 1069–1088. DOI: 10.1093/mnras/199.4.1069.

Elmegreen, B. G. and D. M. Elmegreen (Jan. 1985). "Properties of barred spiral galaxies." In: *The Astrophysical Journal* 288, pp. 438–455. DOI: 10.1086/162810.

Erwin, P. (Jan. 2011). "Double-barred galaxies." In: *Memorie della Societa Astronomica Italiana Supplementi* 18, p. 145.

Erwin, Peter (2005). "Bar Lengths and Their Measurement in Disk Galaxies". In: *Monthly Notices of the Royal Astronomical Society* 364, pp. 283–302.

— (Mar. 2018). "The dependence of bar frequency on galaxy mass, colour, and gas content - and angular resolution - in the local universe". In: *Monthly*

Notices of the Royal Astronomical Society 474.4, pp. 5372–5392. DOI: 10.1093/mnras/stx3117. arXiv: 1711.04867 [astro-ph.GA].

Fathi, K. et al. (Oct. 2009). "PATTERN SPEEDS OF BARS AND SPIRAL ARMS FROM H VELOCITY FIELDS". In: *The Astrophysical Journal* 704.2, pp. 1657–1675. ISSN: 1538-4357. DOI: 10.1088/0004-637x/704/2/1657. URL: http://dx.doi.org/10.1088/0004-637X/704/2/1657.

Gadotti, Dimitri A. (Aug. 2011). "Secular evolution and structural properties of stellar bars in galaxies". In: *Monthly Notices of the Royal Astronomical Society* 415.4, pp. 3308–3318. DOI: 10.1111/j.1365-2966.2011.18945.x. arXiv: 1003.1719 [astro-ph.CO].

Gadotti, Dimitri Alexei (June 2004). "On the Formation and Evolution of Stellar Bars in Galaxies". In: *Publications of the Astronomical Society of the Pacific* 116.820, pp. 591–592. ISSN: 1538-3873. DOI: 10.1086/421709. URL: http://dx.doi.org/10.1086/421709.

García-Burillo, S., F. Combes, and M. Gerin (1993). "Gas dynamics in the barred galaxy NGC 7479". In: *Astronomy & Astrophysics* 274, pp. 148–162.

Garcia-Gómez, C. et al. (May 2017). "Measuring bar strength using Fourier analysis of galaxy images". In: *Astronomy & Astrophysics* 601, A132, A132. DOI: 10.1051/0004-6361/201628830.

Garma-Oehmichen, L et al. (Nov. 2019). "SDSS-IV MaNGA: Bar pattern speed estimates with the Tremaine-Weinberg method and their error sources". In: *Monthly Notices of the Royal Astronomical Society*. ISSN: 1365-2966. DOI: 10.1093/mnras/stz3101. URL: http://dx.doi.org/10.1093/mnras/stz3101.

George, Koshy, Smitha Subramanian, and K. T. Paul (July 2019). "Significance of bar quenching in the global quenching of star formation". In: *Astronomy & Astrophysics* 628, A24. DOI: 10.48550/arXiv.1907.06910. URL: https://arxiv.org/abs/1907.06910.

Géron, Tobias et al. (2025). *Galaxy Zoo CEERS: Bar fractions up to z 4.0*. arXiv: 2505.01421 [astro-ph.GA]. URL: https://arxiv.org/abs/2505.01421.

Gerssen, J., K. Kuijken, and M. R. Merrifield (1999). "Measuring the Pattern Speed of Bars: The Tremaine–Weinberg Method Applied to NGC 4151". In: *Monthly Notices of the Royal Astronomical Society* 306, pp. 327–334. URL: https://ui.adsabs.harvard.edu/abs/1999MNRAS.306..327G.

Gerssen, Joris, Konrad Kuijken, and Michael R. Merrifield (Oct. 2003). "Model-independent measurements of bar pattern speeds". In: *Monthly Notices of the Royal Astronomical Society* 345.1, pp. 261–268. DOI: 10.1046/j.1365-8711.2003.06937.x. URL: https://doi.org/10.1046/j.1365-8711.2003.06937.x.

Ghosh, Soumavo and Paola Di Matteo (Mar. 2024). "Looking for a needle in a haystack: Measuring the length of a stellar bar". In: *Astronomy & Astrophysics* 683, A100, A100. DOI: 10.1051/0004-6361/202347763. arXiv: 2308.10948 [astro-ph.GA].

Ghosh, Soumavo, Francesca Fragkoudi, et al. (Mar. 2024). "Bars and boxy/peanut bulges in thin and thick discs: III. Boxy/peanut bulge formation and evolution in the presence of thick discs". In: *Astronomy Astrophysics* 683, A196.

ISSN: 1432-0746. DOI: 10.1051/0004-6361/202347831. URL: http://dx.doi.org/10.1051/0004-6361/202347831.

Ghosh, Soumavo, Kanak Saha, Paola Di Matteo, et al. (Jan. 2021). "Fate of stellar bars in minor merger of galaxies". In: *Monthly Notices of the Royal Astronomical Society* 502.2, pp. 3085–3100. ISSN: 0035-8711. DOI: 10.1093/mnras/stab238. eprint: https://academic.oup.com/mnras/article-pdf/502/2/3085/36276076/stab238.pdf. URL: https://doi.org/10.1093/mnras/stab238.

Ghosh, Soumavo, Kanak Saha, Chanda J. Jog, et al. (Apr. 2022). "Genesis of morpho-kinematic lopsidedness in minor merger of galaxies". In: *Monthly Notice of the Royal Astronomical Society* 511.4, pp. 5878–5896. DOI: 10.1093/mnras/stac461. arXiv: 2105.05270 [astro-ph.GA].

Ghosh, Soumavo et al. (2023). "Bars and boxy/peanut bulges in thin and thick discs - II. Can bars form in hot thick discs?" In: *Astronomy & Astrophysics* 674, A128. DOI: 10.1051/0004-6361/202245275. URL: https://doi.org/10.1051/0004-6361/202245275.

Guo, Yuchen, Shardha Jogee, Steven L. Finkelstein, et al. (Mar. 2023). "First Look at z gt; 1 Bars in the Rest-frame Near-infrared with JWST Early CEERS Imaging". In: *The Astrophysical Journal Letters* 945.1, p. L10. ISSN: 2041-8213. DOI: 10.3847/2041-8213/acacfb. URL: http://dx.doi.org/10.3847/2041-8213/acacfb.

Guo, Yuchen, Shardha Jogee, Eden Wise, et al. (June 2025). "The Abundance and Properties of Barred Galaxies out to z ∼ 4 Using JWST CEERS Data". In: *The Astrophysical Journal* 985.2, 181, p. 181. DOI: 10.3847/1538-4357/adc8a7. arXiv: 2409.06100 [astro-ph.GA].

Hammersley, P. L. et al. (Sept. 2000). "Detection of the old stellar component of the major Galactic bar". In: *Monthly Notices of the Royal Astronomical Society* 317.3, pp. L45–L49. ISSN: 0035-8711. DOI: 10.1046/j.1365-8711.2000.03858.x. eprint: https://academic.oup.com/mnras/article-pdf/317/3/L45/2900600/317-3-L45.pdf. URL: https://doi.org/10.1046/j.1365-8711.2000.03858.x.

Haynes, Martha P. et al. (Jan. 1998). "Asymmetry in High-Precision Global H i Profiles of Isolated Spiral Galaxies". In: *The Astrophysical Journal* 115.1, pp. 62–79. DOI: 10.1086/300166.

Hernandez, Olivier et al. (2005). "On the Relevance of the Tremaine-Weinberg Method Applied to an H Velocity Field: Pattern Speed Determination in M100 (NGC 4321)". In: *The Astrophysical Journal* 632.1, pp. 253–265. DOI: 10.1086/431964.

Hernquist, Lars and Neal Katz (June 1989). "TREESPH: A Unification of SPH with the Hierarchical Tree Method". In: *The Astrophysical Journal Supplement Series* 70, p. 419. DOI: 10.1086/191344.

Hunter, J. H. et al. (1988). "Gas dynamics in barred spiral galaxies". In: *The Astrophysical Journal* 324, pp. 721–743. DOI: 10.1086/165930.

Jog, Chanda J. and Francoise Combes (Feb. 2009). "Lopsided spiral galaxies". In: *Physics Reports* 471.2, pp. 75–111. DOI: 10.1016/j.physrep.2008.12.002. arXiv: 0811.1101 [astro-ph].

Jogee, Shardha et al. (Nov. 2004). "Bar Evolution over the Last 8 Billion Years: A Constant Fraction of Strong Bars in the GEMS Survey". In: *The Astro-*

physical Journal Letters 615.2, pp. L105–L108. DOI: 10.1086/426138. arXiv: astro-ph/0408382 [astro-ph].

Julian, William H. and Alar Toomre (Dec. 1966). "Non-Axisymmetric Responses of Differentially Rotating Disks of Stars". In: *The Astrophysical Journal* 146, p. 810. DOI: 10.1086/148957.

Kalberla, P. M. W. and L. Dedes (2008). "Global properties of the H I distribution in the outer Milky Way. Planar and extra-planar gas". In: *Astronomy & Astrophysics* 487.3, pp. 951–963. DOI: 10.1051/0004-6361:20079240.

Kennicutt Jr., Robert C. (May 1998). "The Global Schmidt Law in Star-forming Galaxies". In: *The Astrophysical Journal* 498.2, pp. 541–552. DOI: 10.1086/305588. arXiv: astro-ph/9712213 [astro-ph].

Kent, S. M. (June 1986). "Dark matter in spiral galaxies. I. Galaxies with optical rotation curves." In: *The Astronomical Journal* 91, pp. 1301–1327. DOI: 10.1086/114106.

Khochfar, S. and A. Burkert (Jan. 2006). "Orbital parameters of merging dark matter halos". In: *Astronomy & Astrophysics* 445.2, pp. 403–412. DOI: 10.1051/0004-6361:20053241. arXiv: astro-ph/0309611 [astro-ph].

Kormendy, J. and Robert C. Kennicutt (2004). "Secular Evolution and the Growth of Pseudobulges in Disk Galaxies". In: *Annual Review of Astronomy and Astrophysics* 42, pp. 603–683.

Kraljic, Katarina, Frédéric Bournaud, and Marie Martig (Sept. 2012). "THE TWO-PHASE FORMATION HISTORY OF SPIRAL GALAXIES TRACED BY THE COSMIC EVOLUTION OF THE BAR FRACTION". In: *The Astrophysical Journal* 757.1, p. 60. DOI: 10.1088/0004-637X/757/1/60. URL: https://doi.org/10.1088/0004-637X/757/1/60.

Kruk, Sandor J. et al. (May 2017). "Galaxy Zoo: finding offset discs and bars in SDSS galaxies". In: *Monthly Notices of the Royal Astronomical Society* 469.3, pp. 3363–3373. ISSN: 0035-8711. DOI: 10.1093/mnras/stx1026. eprint: https://academic.oup.com/mnras/article-pdf/469/3/3363/17656855/stx1026.pdf. URL: https://doi.org/10.1093/mnras/stx1026.

Laine, S. and C. H. Heller (1999). "Gas dynamics in the barred galaxy NGC 5383". In: *Monthly Notices of the Royal Astronomical Society* 308.3, pp. 557–567. DOI: 10.1046/j.1365-8711.1999.02747.x.

Laurikainen, E., H. Salo, and P. Rautiainen (2002). "Fourier decomposition and bar strength in spiral galaxies". In: *Monthly Notices of the Royal Astronomical Society* 331, pp. 880–895.

Laurikainen, Eija, Heikki Salo, and Ronald Buta (May 2004). "Comparison of Bar Strengths and Fractions of Bars in Active and Nonactive Galaxies". In: *The Astrophysical Journal* 607.1, p. 103. DOI: 10.1086/383462. URL: https://doi.org/10.1086/383462.

— (Oct. 2005). "Multicomponent decompositions for a sample of S0 galaxies". In: *Monthly Notices of the Royal Astronomical Society* 362.4, pp. 1319–1347. DOI: 10.1111/j.1365-2966.2005.09404.x. arXiv: astro-ph/0508097 [astro-ph].

Le Conte, Zoe A et al. (Apr. 2024). "A JWST investigation into the bar fraction at redshifts 1 z 3". In: *Monthly Notices of the Royal Astronomical Society*

530.2, pp. 1984–2000. ISSN: 1365-2966. DOI: 10.1093/mnras/stae921. URL: http://dx.doi.org/10.1093/mnras/stae921.

Lee, Yun Hee et al. (Feb. 2022). "Properties of Fast and Slow Bars Classified by Epicyclic Frequency Curves from Photometry of Barred Galaxies". In: *The Astrophysical Journal* 926.1, p. 58. DOI: 10.3847/1538-4357/ac3bc1. URL: https://doi.org/10.3847/1538-4357/ac3bc1.

Liszt, H. S. and W. B. Burton (Mar. 1980). "The gas distribution in the central region of the galaxy. III - A barlike model of the inner-galaxy gas based on improved H I data." In: *The Astrophysical Journal* 236, pp. 779–797. DOI: 10.1086/157803.

Mahor, Adarsh et al. (2021). *Estimating dynamical parameters of two interacting galaxies using Deep Learning*. arXiv: 2112.12604 [astro-ph.GA]. URL: https://arxiv.org/abs/2112.12604.

Mapelli, M., B. Moore, and J. Bland-Hawthorn (Aug. 2008). "Lopsided galaxies: the case of NGC 891". In: *Monthly Notices of the Royal Astronomical Society* 388.2, pp. 697–708. DOI: 10.1111/j.1365-2966.2008.13421.x. arXiv: 0805.1104 [astro-ph].

Marinova, Irina and Shardha Jogee (Apr. 2007). "Characterizing Bars at z 0 in the Optical and NIR: Implications for the Evolution of Barred Disks with Redshift". In: *The Astrophysical Journal* 659.2, p. 1176. DOI: 10.1086/512355. URL: https://doi.org/10.1086/512355.

Masters, Karen L. et al. (Feb. 2011). "Galaxy Zoo: bars in disc galaxies*". In: *Monthly Notices of the Royal Astronomical Society* 411.3, pp. 2026–2034. ISSN: 0035-8711. DOI: 10.1111/j.1365-2966.2010.17834.x. eprint: https://academic.oup.com/mnras/article-pdf/411/3/2026/2955962/mnras0411-2026.pdf. URL: https://doi.org/10.1111/j.1365-2966.2010.17834.x.

Meidt, Sharon E. et al. (2009). "Radial Variation of Spiral Pattern Speed in M51". In: *The Astrophysical Journal* 702.1, pp. 277–285. DOI: 10.1088/0004-637X/702/1/277.

Melvin, Thomas et al. (Jan. 2014). "Galaxy Zoo: an independent look at the evolution of the bar fraction over the last eight billion years from HST-COSMOS". In: *Monthly Notices of the Royal Astronomical Society* 438.4, pp. 2882–2897.

Menendez-Delmestre, Karin et al. (Mar. 2007). "A Near-Infrared Study of 2MASS Bars in Local Galaxies: An Anchor for High-Redshift Studies". In: *The Astrophysical Journal* 657.2, pp. 790–804. DOI: 10.1086/511025.

Merrifield, Michael R. and Konrad Kuijken (June 1995). "The pattern speed of the bar in NGC 936". In: *Monthly Notices of the Royal Astronomical Society* 274.3, pp. 933–938. DOI: 10.1093/mnras/274.3.933. eprint: astro-ph/9502069. URL: https://ui.adsabs.harvard.edu/abs/1995MNRAS.274..933M.

Miyamoto, M. and R. Nagai (Dec. 1975). "Three-Dimensional Models for the Distribution of Mass in Galaxies". In: *Publications of the Astronomical Society of Japan* 27.4, pp. 533–543. DOI: 10.1093/pasj/27.4.533.

Montuori, M. et al. (July 2010). "The dilution peak, metallicity evolution, and dating of galaxy interactions and mergers". In: *Astronomy & Astrophysics*

518, A56, A56. DOI: 10.1051/0004-6361/201014304. arXiv: 1003.1374 [astro-ph.CO].

Nair, Preethi B. and Roberto G. Abraham (May 2010). "On the Fraction of Barred Spiral Galaxies". In: *The Astrophysical Journal Letters* 714.2, pp. L260–L264. DOI: 10.1088/2041-8205/714/2/L260. arXiv: 1004.0684 [astro-ph.CO].

Noordermeer, E. et al. (Oct. 2005). "The Westerbork HI survey of spiral and irregular galaxies. III. HI observations of early-type disk galaxies". In: *Astronomy & Astrophysics* 442.1, pp. 137–157. DOI: 10.1051/0004-6361:20053172. arXiv: astro-ph/0508319 [astro-ph].

Noordermeer, Edo, Linda S. Sparke, and Stephen E. Levine (Dec. 2001). "The kinematics of lopsided galaxies". In: *Monthly Notices of the Royal Astronomical Society* 328.4, pp. 1064–1080. DOI: 10.1046/j.1365-8711.2001.04924.x. arXiv: astro-ph/0112305 [astro-ph].

Ohta, K., M. Hamabe, and K.-I. Wakamatsu (1990). "Structure and dynamics of barred galaxies Fourier decomposition of galaxy images". In: *The Astrophysical Journal* 357, pp. 71–82.

Ostriker, J. P. and P. J. E. Peebles (Dec. 1973). "A Numerical Study of the Stability of Flattened Galaxies: or, can Cold Galaxies Survive?" In: *The Astrophysical Journal* 186, pp. 467–480. DOI: 10.1086/152513.

Phookun, Bikram and Lee G. Mundy (Nov. 1995). "NGC 4654: A Virgo Cluster Spiral Interacting with the Intracluster Medium". In: *The Astrophysical Journal* 453, p. 154. DOI: 10.1086/176376.

Plummer, H. C. (Mar. 1911). "On the problem of distribution in globular star clusters". In: *Monthly Notices of the Royal Astronomical Society* 71, pp. 460–470. DOI: 10.1093/mnras/71.5.460.

Prakash, Prem, Arunima Banerjee, and Pavan Kumar Perepu (July 2020). "Determination of the relative inclination and the viewing angle of an interacting pair of galaxies using Convolutional Neural Networks". In: *Monthly Notices of the Royal Astronomical Society* 497.3, pp. 3323–3334. ISSN: 1365-2966. DOI: 10.1093/mnras/staa2109. URL: http://dx.doi.org/10.1093/mnras/staa2109.

Prasad, Chaitanya and Chanda J. Jog (Apr. 2017). "Off-center dark matter halo leading to strong central disk lopsidedness". In: *Astronomy & Astrophysics* 600, A17, A17. DOI: 10.1051/0004-6361/201630071. arXiv: 1610.01702 [astro-ph.GA].

Raha, N. et al. (Aug. 1991). "A dynamical instability of bars in disk galaxies". In: *Nature* 352.6334, pp. 411–412. DOI: 10.1038/352411a0.

Rand, R. J. (1995). "The Kinematics of Ionized Gas in NGC 1068". In: *The Astronomical Journal* 109, p. 2444. URL: https://ui.adsabs.harvard.edu/abs/1995AJ....109.2444R.

Randriamampandry, T. H. et al. (Oct. 2016). "Exploring the GalMer database: bar properties and non-circular motions". In: *Astronomy & Astrophysics* 594, A86, A86. DOI: 10.1051/0004-6361/201629081. arXiv: 1608.00690 [astro-ph.GA].

Rautiainen, P., H. Salo, and E. Laurikainen (2008). "Comparison of observed barred galaxy morphologies with numerical simulations". In: *Monthly No-*

tices of the Royal Astronomical Society 388.4, pp. 1803–1814. DOI: 10.1111/j.1365-2966.2008.13516.x.

Reichard, T. A. et al. (2008). "Lopsided Galaxies in the Sloan Digital Sky Survey". In: *The Astrophysical Journal* 677, pp. 186–199. URL: https://ui.adsabs.harvard.edu/abs/2008ApJ...677..186R.

Reichard, Timothy A. et al. (Apr. 2008). "The Lopsidedness of Present-Day Galaxies: Results from the Sloan Digital Sky Survey". In: *The Astrophysical Journal* 677.1, pp. 186–200. DOI: 10.1086/526506. eprint: 0710.0589. URL: https://ui.adsabs.harvard.edu/abs/2008ApJ...677..186R.

Richter, O. -G. and R. Sancisi (Oct. 1994). "Asymmetries in disk galaxies. How often? How strong?" In: *Astronomy & Astrophysics* 290, pp. L9–L12.

Rix, Hans-Walter and Dennis Zaritsky (July 1995). "Nonaxisymmetric Structures in the Stellar Disks of Galaxies". In: *The Astrophysical Journal* 447, p. 82. DOI: 10.1086/175858. eprint: astro-ph/9505111. URL: https://ui.adsabs.harvard.edu/abs/1995ApJ...447...82R.

Romero-Gómez, M. et al. (July 2019). "Gaia kinematics reveal a complex lopsided and twisted Galactic disc warp". In: *Astronomy & Astrophysics* 627, A150, A150. DOI: 10.1051/0004-6361/201834908. eprint: 1812.07576. URL: https://ui.adsabs.harvard.edu/abs/2019A&A...627A.150R.

Rosas-Guevara, Yetli et al. (Mar. 2022). "The evolution of the barred galaxy population in the TNG50 simulation". In: *Monthly Notices of the Royal Astronomical Society* 512.4, pp. 5339–5357. ISSN: 1365-2966. DOI: 10.1093/mnras/stac816. URL: http://dx.doi.org/10.1093/mnras/stac816.

Saha, K., R. S. de Jong, and B. W. Holwerda (2009). "On the Origin of Warps and Lopsidedness in Disk Galaxies". In: *Monthly Notices of the Royal Astronomical Society* 396, pp. 409–422. URL: https://ui.adsabs.harvard.edu/abs/2009MNRAS.396..409S.

Saha, Kanak, Francoise Combes, and Chanda J. Jog (Nov. 2007). "Global lopsided instability in a purely stellar galactic disc". In: *Monthly Notices of the Royal Astronomical Society* 382.1, pp. 419–432. DOI: 10.1111/j.1365-2966.2007.12382.x. arXiv: 0708.2873 [astro-ph].

Saha, Kanak, Yao-Huan Tseng, and Ronald E. Taam (2010). "The Effect of Bars and Transient Spirals on the Vertical Heating in Disk Galaxies". In: *The Astrophysical Journal* 721.2, pp. 1878–1890. DOI: 10.1088/0004-637X/721/2/1878.

Salo, H. et al. (May 2010). "BARS DO DRIVE SPIRAL DENSITY WAVES". In: *The Astrophysical Journal Letters* 715.1, p. L56. DOI: 10.1088/2041-8205/715/1/L56. URL: https://doi.org/10.1088/2041-8205/715/1/L56.

Sánchez, S. F., R. C. Kennicutt, A. Gil de Paz, et al. (2012). "CALIFA, the Calar Alto Legacy Integral Field Area survey. I. Survey presentation". In: *Astronomy & Astrophysics* 538, A8. DOI: 10.1051/0004-6361/201117353.

Sanders, R. H. and A. D. Tubbs (1980). "The morphology of barred galaxies. I - Models". In: *The Astrophysical Journal* 235, pp. 803–819. DOI: 10.1086/157683.

Schmidt, Maarten (Mar. 1959). "The Rate of Star Formation." In: *The Astrophysical Journal* 129, p. 243. DOI: 10.1086/146614.

Schoenmakers, R. H. M., M. Franx, and P. T. de Zeeuw (Dec. 1997). "Measuring non-axisymmetry in spiral galaxies". In: *Monthly Notices of the Royal Astronomical Society* 292.2, pp. 349–364. DOI: 10.1093/mnras/292.2.349. arXiv: astro-ph/9707332 [astro-ph].

Sellwood, J A and A Wilkinson (Feb. 1993). "Dynamics of barred galaxies". In: *Reports on Progress in Physics* 56.2, p. 173. DOI: 10.1088/0034-4885/56/2/001. URL: https://doi.org/10.1088/0034-4885/56/2/001.

Sellwood, J. A. (May 1989). "Meta-stability in galactic discs". In: *Monthly Notice of the Royal Astronomical society* 238, pp. 115–131. DOI: 10.1093/mnras/238.1.115.

— (May 2012). "SPIRAL INSTABILITIES IN N-BODY SIMULATIONS. I. EMERGENCE FROM NOISE". In: *The Astrophysical Journal* 751.1, p. 44. DOI: 10.1088/0004-637X/751/1/44. URL: https://doi.org/10.1088/0004-637X/751/1/44.

— (Jan. 2014). "Secular evolution in disk galaxies". In: *Reviews of Modern Physics* 86.1, pp. 1–46. DOI: 10.1103/RevModPhys.86.1. arXiv: 1310.0403 [astro-ph.GA].

Semelin, B. and F. Combes (June 2002). "Formation and evolution of galactic disks with a multiphase numerical model". In: *Astronomy Astrophysics* 388, pp. 826–841. DOI: 10.1051/0004-6361:20020547. arXiv: astro-ph/0204240 [astro-ph].

Sheth, Kartik et al. (Mar. 2008). "Evolution of the Bar Fraction in COSMOS: Quantifying the Assembly of the Hubble Sequence". In: *The Astrophysical Journal* 675.2, p. 1141. DOI: 10.1086/524980. URL: https://doi.org/10.1086/524980.

Sormani, Mattia C., James Binney, and John Magorrian (Apr. 2015). "Gas flow in barred potentials". In: *Monthly Notices of the Royal Astronomical Society* 449.3, pp. 2421–2435. ISSN: 0035-8711. DOI: 10.1093/mnras/stv441. URL: http://dx.doi.org/10.1093/mnras/stv441.

Spinoso, Daniele et al. (2016). "Bar-driven evolution and quenching of spiral galaxies in cosmological simulations". In: *Monthly Notices of the Royal Astronomical Society* 465, pp. 3729–3740. URL: https://api.semanticscholar.org/CorpusID:119103980.

Springel, Volker (Dec. 2005). "The cosmological simulation code gadget-2". In: *Monthly Notices of the Royal Astronomical Society* 364.4, pp. 1105–1134. ISSN: 1365-2966. DOI: 10.1111/j.1365-2966.2005.09655.x. URL: http://dx.doi.org/10.1111/j.1365-2966.2005.09655.x.

Swaters, R. A. et al. (Apr. 1999). "Kinematically lopsided spiral galaxies". In: *Monthly Notices of the Royal Astronomical Society* 304.2, pp. 330–334. DOI: 10.1046/j.1365-8711.1999.02332.x. arXiv: astro-ph/9811424 [astro-ph].

Toomre, A. (May 1964). "On the gravitational stability of a disk of stars." In: *The Astrophysical Journal* 139, pp. 1217–1238. DOI: 10.1086/147861.

— (Jan. 1981). "What amplifies the spirals". In: *Structure and Evolution of Normal Galaxies*. Ed. by S. M. Fall and D. Lynden-Bell, pp. 111–136.

Tremaine, S. and M. D. Weinberg (July 1984). "A kinematic method for measuring the pattern speed of barred galaxies." In: *The Astrophysical Journal Let-*

ters 282, pp. L5–L7. DOI: 10.1086/184292. URL: https://ui.adsabs.harvard.edu/abs/1984ApJ...282L...5T.

van Eymeren, J. et al. (June 2011). "Lopsidedness in WHISP galaxies. II. Morphological lopsidedness". In: *Astronomy & Astrophysics* 530, A30, A30. DOI: 10.1051/0004-6361/201016178. eprint: 1103.4929. URL: https://ui.adsabs.harvard.edu/abs/2011A&A...530A..30V.

Wegg, Christopher and Ortwin Gerhard (Sept. 2013). "Mapping the three-dimensional density of the Galactic bulge with VVV red clump stars". In: *Monthly Notices of the Royal Astronomical Society* 435.3, pp. 1874–1887. ISSN: 0035-8711. DOI: 10.1093/mnras/stt1376. eprint: https://academic.oup.com/mnras/article-pdf/435/3/1874/3346310/stt1376.pdf. URL: https://doi.org/10.1093/mnras/stt1376.

Weiner, B. J., J. A. Sellwood, and T. B. Williams (2001). "Bar pattern speeds in gas-rich galaxies". In: *The Astrophysical Journal* 546, pp. 931–949. DOI: 10.1086/318300.

Zaritsky, Dennis and Hans-Walter Rix (Mar. 1997). "Lopsided Spiral Galaxies and a Limit on the Galaxy Accretion Rate". In: *The Astrophysical journal* 477.1, pp. 118–127. DOI: 10.1086/303692. arXiv: astro-ph/9608086 [astro-ph].

Zaritsky, Dennis, Heikki Salo, et al. (Aug. 2013). "On the Origin of Lopsidedness in Galaxies as Determined from the Spitzer Survey of Stellar Structure in Galaxies (S^4G)". In: *The Astrophysical Journal* 772.2, p. 135. DOI: 10.1088/0004-637X/772/2/135. eprint: 1305.2940. URL: https://ui.adsabs.harvard.edu/abs/2013ApJ...772..135Z.

Zou, Yanfei et al. (Oct. 2019). "Testing the Tremaine–Weinberg Method Applied to Integral-field Spectroscopic Data Using a Simulated Barred Galaxy". In: *The Astrophysical Journal* 884.1, p. 23. ISSN: 1538-4357. DOI: 10.3847/1538-4357/ab3f34. URL: http://dx.doi.org/10.3847/1538-4357/ab3f34.